Measurements of single and double spin asymmetry in pp elastic scattering in the CNI region with a polarized atomic hydrogen gas jet target

I. G. Alekseev,[4] A. Bravar,[1,*] G. Bunce,[1,2] S. Dhawan,[8] K. O. Eyser,[9,†] R. Gill,[1] W. Haeberli,[7] H. Huang,[1] O. Jinnouchi,[2,‡] A. Kponou,[1] Y. Makdisi,[1] I. Nakagawa,[10] A. Nass,[1,§] H. Okada,[5,‖] N. Saito,[5,‡] E. J. Stephenson,[3] D. N. Svirida,[4] T. Wise,[7] J. Wood,[1,¶] and A. Zelenski[1]

[1]*Brookhaven National Laboratory, Upton, New York 11973, USA*
[2]*RIKEN BNL Research Center, Upton, New York 11973, USA*
[3]*Indiana University Cyclotron Facility, Bloomington, Indiana 47408, USA*
[4]*Institute for Theoretical and Experimental Physics (ITEP), 117259 Moscow, Russia*
[5]*Kyoto University, Sakyo-ku, Kyoto 606-8502, Japan, and RIKEN, Wako, Saitama 351-0198, Japan*
[6]*Stony Brook University, Stony Brook, New York 11794, USA*
[7]*University of Wisconsin, Madison, Wisconsin 53706, USA*
[8]*Yale University, New Haven, Connecticut 06520, USA*
[9]*University of California, Riverside, California 92521, USA*
[10]*RIKEN, Wako, Japan*

(Received 14 June 2008; published 13 May 2009)

Precise measurements of the single spin asymmetry A_N, and the double spin asymmetry A_{NN}, in proton-proton (pp) elastic scattering in the region of four-momentum transfer squared $0.001 < -t < 0.032$ $(\mathrm{GeV}/c)^2$ have been performed using a polarized atomic hydrogen gas jet target and the Relativistic Heavy Ion Collider (RHIC) polarized proton beam. We present measurements of A_N and A_{NN} at center-of-mass energies $\sqrt{s} = 6.8$ and 13.7 GeV. These spin-dependent observables are sensitive to the poorly known hadronic spin-dependent amplitudes. Comparing A_N at different energies, a $\sqrt{s}$ dependence of the hadronic single spin-flip amplitude is suggested. A hadronic double spin-flip amplitude from the A_{NN} data is consistent with zero within a 2-σ level. We also present $\Delta\sigma_T$, estimated from the measured A_{NN} data. The results for $\Delta\sigma_T$ are consistent with zero. Our results provide significant constraints toward a comprehensive understanding of the reaction mechanism for pp elastic scattering.

DOI: 10.1103/PhysRevD.79.094014 PACS numbers: 13.88.+e, 13.85.Dz, 29.25.Pj

I. INTRODUCTION

Measurements of proton-proton (pp) elastic scattering have been a basic tool toward understanding the strong interaction. The total pp cross section (σ_{tot}) has been measured over a large energy range, for center-of-mass energies to $\sqrt{s} = 40$ TeV with the surprising result that the cross section rises approximately as $\ln^2 s$ for $\sqrt{s} > 20$ GeV. The Regge pole exchange model describes this cross section well for $\sqrt{s} \geq 5$ GeV. It was necessary to introduce the Pomeron to describe the rising cross section. In more modern terms, the Pomeron is often described as multigluon exchange [1]. These measurements and their description have generally been for unpolarized (spin-averaged) scattering.

The addition of spin-dependent scattering results probes nonperturbative quantum chromodynamics (QCD) in new ways. Spin asymmetries are a fully quantum mechanical effect, directly probing the amplitudes of the scattering process. An interference between amplitudes, which involve helicity flip at the amplitude level, is necessary to generate a spin asymmetry. In particular, a small helicity-flip amplitude can give little contribution to an unpolarized cross section, but can result in a significant spin asymmetry. Therefore the measurement of spin asymmetry provides sensitive direct information on helicity-dependent scattering amplitudes, for example, on the spin dependence of the Pomeron exchange.

The transition amplitude for nucleon-nucleon scattering $A + B \rightarrow C + D$ is described in the center-of-mass system by a matrix ϕ in spin space as

$$\phi(s, t) = \langle \lambda_C \lambda_D | \phi | \lambda_A \lambda_B \rangle, \tag{1}$$

where λ_A and λ_B (λ_C and λ_D) correspond to the initial (final) helicity states. Requiring that the interaction is invariant under space inversion, time reversal, and for identical particles, pp scattering in a given initial and final spin state is described by five independent transition am-

*Present address: University of Geneva, 1205 Geneva, Switzerland.
†Present address: Deutsches Elektronen Synchrotron, 22607 Hamburg, Germany.
‡Present address: KEK, Tsukuba, Ibaraki 305-0831, Japan.
§Present address: University of Erlangen-Nurenberg, Erwin-Rommel-Strasse 1, 91058 Erlangen, Germany.
‖Contact person, email address: hiromi@post.kek.jp, okadah@bnl.gov; Present address: KEK, Tsukuba, Ibaraki 305-0831, Japan.
¶Present address: United States Nuclear Regulatory Commission, Washington, DC 20555-0001, USA.

plitudes, functions of the center-of-mass energy squared s, and the four-momentum transfer squared $-t(\geq 0)$ [2].

$$\begin{aligned}
\phi_1(s,t) &= \langle +\tfrac{1}{2} + \tfrac{1}{2}|\phi| + \tfrac{1}{2} + \tfrac{1}{2}\rangle, \\
\phi_2(s,t) &= \langle +\tfrac{1}{2} + \tfrac{1}{2}|\phi| - \tfrac{1}{2} - \tfrac{1}{2}\rangle, \\
\phi_3(s,t) &= \langle +\tfrac{1}{2} - \tfrac{1}{2}|\phi| + \tfrac{1}{2} - \tfrac{1}{2}\rangle, \\
\phi_4(s,t) &= \langle +\tfrac{1}{2} - \tfrac{1}{2}|\phi| - \tfrac{1}{2} + \tfrac{1}{2}\rangle, \\
\phi_5(s,t) &= \langle +\tfrac{1}{2} + \tfrac{1}{2}|\phi| + \tfrac{1}{2} - \tfrac{1}{2}\rangle.
\end{aligned} \tag{2}$$

$\phi_1(s,t)$ and $\phi_3(s,t)$ correspond to non-spin-flip amplitudes and it is convenient to define

$$\phi_+(s,t) \equiv \tfrac{1}{2}(\phi_1(s,t) + \phi_3(s,t)). \tag{3}$$

$\phi_5(s,t)$ corresponds to a single-spin-flip amplitude. $\phi_2(s,t)$ and $\phi_4(s,t)$ correspond to double-spin-flip amplitudes. In the region where $\sqrt{s}$ is sufficiently larger than the proton mass M_p and $-t$ is very small, less than 0.05 $(\mathrm{GeV}/c)^2$ [3], each transition amplitude can be written as $\phi_1(s,t) \to \phi_1^{\mathrm{had}}(s,t) + e^{i\delta_C}\phi_1^{\mathrm{em}}(s,t)$ with hadronic and electromagnetic elements, at the lowest order in the fine structure constant, α. The Coulomb phase $\delta_C \sim 0.02$ is independent of helicity [4,5]. The five Coulomb elements $\phi_i^{\mathrm{em}}(s,t)$ $(i = 1\text{–}5)$ are predicted by quantum electrodynamics (QED), including their spin dependence.

The hadronic elements, on the other hand, include theoretical uncertainties except for $\phi_+^{\mathrm{had}}(s,t)$. $\phi_+^{\mathrm{had}}(s,t)$ is related to the unpolarized differential cross section, which is measured precisely in the region of $-t < 0.1$ $(\mathrm{GeV}/c)^2$ [6],

$$\begin{aligned}
\frac{d\sigma}{dt} &= \frac{2\pi}{s^2}\{|\phi_1(s,t)|^2 + |\phi_2(s,t)|^2 + |\phi_3(s,t)|^2 \\
&\quad + |\phi_4(s,t)|^2 + 4|\phi_5(s,t)|^2\} \\
&\cong \frac{4\pi}{s^2}|\phi_+^{\mathrm{had}}(s,t) + \phi_+^{\mathrm{em}}(s,t)|^2,
\end{aligned} \tag{4}$$

here we assume that $|\phi_2(s,t)|^2$, $|\phi_4(s,t)|^2$, and $|\phi_5(s,t)|^2$ are small compared to $|\phi_+(s,t)|^2$ [7–9] and are discussed later. In the limit at $-t = 0$, the imaginary part of $\phi_+^{\mathrm{had}}(s,0)$ is directly related to the total cross section via the optical theorem,

$$\sigma_{\mathrm{tot}} = \frac{8\pi}{\sqrt{s(s-4M_p^2)}}\,\mathrm{Im}\,\phi_+(s,0). \tag{5}$$

The kinematic dependence of the remaining three hadronic amplitudes at small $|t|$ can be obtained using angular momentum conservation. The helicity dependence of the hadronic amplitude is described [2]:

$$\phi_i^{\mathrm{had}}(s,t) \propto (-t)^{(1/2)|\lambda_D - \lambda_C - \lambda_B + \lambda_A|}, \tag{6}$$

where i = 2, 4, 5 and corresponding helicity states are shown in (2). For $-t \to 0$, $\phi_4^{\mathrm{had}}(s,t)$ and $\phi_5^{\mathrm{had}}(s,t)$ vanish as $\phi_4^{\mathrm{had}}(s,t) \propto -t$ and $\phi_5^{\mathrm{had}}(s,t) \propto \sqrt{-t}$, while the amplitude $\phi_2^{\mathrm{had}}(s,t)$ has no required $|t|$ dependence. However, there is no prediction for the magnitudes of $\phi_2^{\mathrm{had}}(s,t)$, $\phi_4^{\mathrm{had}}(s,t)$, and $\phi_5^{\mathrm{had}}(s,t)$.

There are several theoretical approaches; models based on eikonalization techniques by Selyugin [10], a diquark enhanced picture of the proton by Kopeliovich and Zakharov [11], an impact model based on the rotating matter picture for a polarized proton (the spin-orbit coupling provides a helicity-flip amplitude) by Bourrely, Soffer, and Wu [12,13]. Their recent predictions are shown in [14]. In this paper we extract parameters in a theoretical framework based on the Regge exchange picture, discussed by Trueman [15]. In this picture, the strong interaction force is due to the exchange of Regge poles, and the exchanges predict the high energy behavior of the transition amplitudes. For pp elastic scattering, five Regge poles (the Pomeron and the dominant charge $(C) = \pm 1$ poles for isospin $(I) = 0, 1$) describe the hadronic part of the transition amplitudes [16]. But their spin dependence, in particular the Pomeron coupling, is unknown. Moreover, Regge pole contributions to $\phi_2^{\mathrm{had}}(s,t)$ near $-t = 0$ are suppressed. This is due to parity conservation of the hadronic interaction, which requires that, for Regge exchange where the vertices for the two interacting protons factorize, $\phi_2^{\mathrm{had}}(s,t) = \phi_4^{\mathrm{had}}(s,t)$, and that $\phi_4^{\mathrm{had}}(s,t)$ vanishes as $|t|$ as $-t \to 0$. This result assumes factorization, and would predict a small double-spin asymmetry A_{NN}, as discussed below. However, if factorization is broken, for example by initial or final state interactions, the amplitude $\phi_2^{\mathrm{had}}(s,t)$ and the double-spin asymmetry A_{NN} can be larger.

The introduction of Regge cuts [17], which break factorization, could result in a significant double-spin asymmetry. A Regge cut corresponds to the simultaneous exchange of two or more Regge poles. In this case, $\phi_2^{\mathrm{had}}(s,t)$ and $\phi_4^{\mathrm{had}}(s,t)$ can behave independently as $-t \to 0$, and $\phi_2^{\mathrm{had}}(s,t)$ would not be required to vanish as $|t| \to 0$.

Note that, as presented below, a large $\phi_2^{\mathrm{had}}(s,t)$ has been observed at low energy. Also, a C-parity-odd exchange, referred to as the Odderon, would also result in nonzero ϕ_2^{had} and A_{NN}.

A nonzero hadronic double-spin-flip amplitude $\phi_2^{\mathrm{had}}(s,t)$ results in a double-spin asymmetry, A_{NN}. The hadronic single-spin-flip amplitude $\phi_5^{\mathrm{had}}(s,t)$ directly modifies the single-spin asymmetry, A_N, from the purely electromagnetic prediction. This paper presents results for these two observables. Their connection to the scattering amplitude is now described.

A. A_N and $\phi_5^{\mathrm{had}}(s,t)$

The nuclear force dominates the pp scattering process except for the very forward kinematic region of $0.001 < -t < 0.1$ $(\mathrm{GeV}/c)^2$. In this region, the electromagnetic force and the nuclear force are similar in strength and their interference term reaches a maximum. This scattering region is referred to as the Coulomb Nuclear Interference

(CNI) region, and a sizable transverse single spin-dependent asymmetry A_N is predicted from an interference of the electromagnetic spin-flip amplitude and the hadronic non-spin-flip amplitude. The definition of A_N is the ratio of the difference and the sum of the differential cross section with the beam or target proton spin up and down:

$$A_N = \frac{d\sigma_{\uparrow 0} - d\sigma_{\downarrow 0}}{d\sigma_{\uparrow 0} + d\sigma_{\downarrow 0}} = -\frac{d\sigma_{0\uparrow} - d\sigma_{0\downarrow}}{d\sigma_{0\uparrow} + d\sigma_{0\downarrow}}. \quad (7)$$

The two subscripts of $d\sigma_{BT}$ denote the beam polarization state (B) and the target polarization state (T). $\uparrow$ ($\downarrow$) define beam or target polarized up (down) in a direction perpendicular to the beam momentum direction. A "0" subscript denotes an unpolarized state. Following the Basel convention [18], we define positive A_N as observing more *forward* scattered protons to the left of the beam (i.e. more *recoil* protons to the beam right), when the beam polarization is up. A significant nonzero A_N in the CNI region was first predicted at the advent of QED by Schwinger [19] for *neutron-nucleus* scattering.

Using the scattering amplitudes of (2), A_N can be expressed as

$$\begin{aligned} A_N \frac{d\sigma}{dt} &= -\frac{4\pi}{s^2}\,\mathrm{Im}[\phi_5^*(s,t)\{\phi_+(s,t) + \phi_2(s,t) \\ &\quad - \phi_4(s,t)\}] \\ &\cong -\frac{4\pi}{s^2}\,\mathrm{Im}[\phi_5^{\mathrm{em}*}(s,t)\phi_+^{\mathrm{had}}(s,t) \\ &\quad + \phi_5^{\mathrm{had}*}(s,t)\phi_+^{\mathrm{em}}(s,t)]. \end{aligned} \quad (8)$$

We assume that $\phi_2^{\mathrm{had}}(s,t)$ and $\phi_4^{\mathrm{had}}(s,t)$ are small compared to $\phi_+^{\mathrm{had}}(s,t)$ [7–9].

The first interference term, $\mathrm{Im}[\phi_5^{\mathrm{em}*}(s,t)\phi_+^{\mathrm{had}}(s,t)]$, in (8) is calculable, with a peak of $A_N \approx 0.04 - 0.05$ around $-t \simeq 0.003$ $(\mathrm{GeV}/c)^2$ over a wide energy range of $\sqrt{s} =$ 10–200 GeV. In the lowest order in the fine structure constant α at high energies, an electromagnetic part of the single-spin-flip amplitude is generated by the proton's anomalous magnetic moment κ as $\phi_5^{\mathrm{em}}(s,t) \cong -s\alpha\kappa/(2M_P\sqrt{-t})$ [4]. The unknown $\phi_5^{\mathrm{had}}(s,t)$ is in the second term and magnified by $\phi_+^{\mathrm{em}} \cong s\alpha/t$ in the lowest order in α. This term would introduce a deviation in shape if the magnitude of $\phi_5^{\mathrm{had}}(s,t)$ is finite. A measurement of A_N in the CNI region, therefore, can be a sensitive probe for $\phi_5^{\mathrm{had}}(s,t)$. An initial measurement of A_N in the CNI region $0.0015 < -t < 0.05$ $(\mathrm{GeV}/c)^2$ was performed by the E704 experiment at $\sqrt{s} = 19.4$ GeV with moderate precision [20]. Recently an A_N measurement in the region $0.01 < -t < 0.03$ $(\mathrm{GeV}/c)^2$ at $\sqrt{s} = 200$ GeV was reported by the PP2PP experiment [21], using the RHIC colliding polarized proton beams.

A precise measurement of the analyzing power A_N in pp elastic scattering in the region of $0.001 < -t < 0.032$ $(\mathrm{GeV}/c)^2$ has been reported using a polarized atomic hydrogen gas jet target and the 100 GeV/c RHIC proton beam ($\sqrt{s} = 13.7$ GeV) [22]. The data are well described by the first term in (8) alone and do not require the presence of a significant hadronic single-spin-flip amplitude, $\phi_5^{\mathrm{had}}(s,t)$. On the other hand, the A_N results for *proton-carbon* (pC) scattering in the CNI region at $\sqrt{s} =$ 6.8 GeV [23] and $\sqrt{s} = 13.7$ GeV[24,25] require a significant hadronic single-spin-flip amplitude to describe the data. The presence of a hadronic single-spin-flip amplitude for pC scattering and absence for pp scattering at $\sqrt{s} =$ 13.7 GeV led to a theoretical prediction of $\sqrt{s}$ dependence for the hadronic single-spin-flip amplitude $\phi_5^{\mathrm{had}}(s,t)$ for pp scattering. This theoretical model predicted a cancellation of $\phi_5^{\mathrm{had}}(s,t)$ at $\sqrt{s} = 13.7$ GeV, and a significant value for $\sqrt{s} = 6.8$ GeV for pp elastic scattering [15].

B. A_{NN} and $\phi_2^{\mathrm{had}}(s,t)$

The double transverse-spin-dependent asymmetry A_{NN} is defined by the ratio of the difference and the sum of the differential cross section with parallel and antiparallel beam/target spin directions:

$$A_{NN} = \frac{(d\sigma_{\uparrow\uparrow} + d\sigma_{\downarrow\downarrow}) - (d\sigma_{\uparrow\downarrow} + d\sigma_{\downarrow\uparrow})}{d\sigma_{\uparrow\uparrow} + d\sigma_{\downarrow\downarrow} + d\sigma_{\uparrow\downarrow} + d\sigma_{\downarrow\uparrow}}. \quad (9)$$

A_{NN} is expressed using the transition amplitudes (2) as

$$\begin{aligned} A_{NN} \frac{d\sigma}{dt} &= \frac{4\pi}{s^2}\{2|\phi_5(s,t)|^2 + \mathrm{Re}[\phi_1^*(s,t)\phi_2(s,t) \\ &\quad - \phi_3^*(s,t)\phi_4(s,t)]\} \\ &\cong \frac{4\pi}{s^2}\{2|\phi_5^{\mathrm{had}}(s,t)|^2 + \mathrm{Re}[(\phi_+^{\mathrm{had}*}(s,t) \\ &\quad + \phi_+^{\mathrm{em}*}(s,t))\phi_2^{\mathrm{had}}(s,t)]\}. \end{aligned} \quad (10)$$

A_{NN} contains $\mathrm{Re}[\phi_+^{\mathrm{em}*}(s,t)\phi_2^{\mathrm{had}}(s,t)]$ and this term is enhanced at small $-t$ due to the Coulomb nuclear interference. Therefore, A_{NN} is sensitive to $\phi_2^{\mathrm{had}}(s,t)$ [26,27].

A_{NN} has been measured at low energy, $\sqrt{s} < 5$ GeV and larger $-t > 1$ $(\mathrm{GeV}/c)^2$ in the 1970s. These experiments studied spin effects in differential cross sections between transverse spin-parallel and spin-antiparallel proton beams around $-t \sim 3.7$ $(\mathrm{GeV}/c)^2$ using the argonne zero gradient synchrotron (ZGS) polarized proton beam at a laboratory momentum 11.75 GeV/c incident on a polarized target [28]. A very large asymmetry was observed with $A_{NN} \approx 0.6$, corresponding to spin parallel to antiparallel total cross sections ratio of $\sigma_{\mathrm{tot}}^{\uparrow\uparrow}/\sigma_{\mathrm{tot}}^{\uparrow\downarrow} \approx 4$. Since then, A_{NN} has been measured for incident proton beam momenta from 0.1 GeV/c to 17.5 GeV/c, covering $\theta_{\mathrm{cm}} = 90°$, and the data show striking structure. The large A_{NN} were predicted to disappear as $-t \to 0$ and $\sqrt{s} \to \infty$ [29].

There had been no experimental result for higher $\sqrt{s}$ and very small $-t$. Recently an A_{NN} measurement in the region $0.01 < -t < 0.03$ $(\mathrm{GeV}/c)^2$ at $\sqrt{s} = 200$ GeV was reported [30] by the PP2PP experiment, using the RHIC colliding polarized proton beams. To reach small $-t$, the

accelerator lattice was used to measure the forward-scattered protons. For experiments using a fixed target in the laboratory (vs. colliding beams), a recoil technique was pioneered at the JINR (Joint Institute for Nuclear Research, Dubna, Russia) using a polarized fixed target [31], to allow access to smaller $-t$, where the forward-scattered particle remains within the beam. The technique is limited by absorption of the recoil particles in the target material. In the case of the results reported in this paper, the gaseous proton target, which results in no absorption of the recoil, is essential to measure elastic scattering in the CNI region.

II. EXPERIMENT

The experiment was performed in 2004 using a polarized atomic hydrogen gas jet target (H-Jet target) and the polarized RHIC proton beam at two momenta, 24 GeV/c ($\sqrt{s} = 6.8$ GeV) and 100 GeV/c ($\sqrt{s} = 13.7$ GeV) [22,32].

A. RHIC beam

The RHIC beam was injected and stored in the RHIC storage rings using individual bunches of $\sim 10^{11}$ protons per bunch. The stable polarization direction was vertical, due to the pair of siberian snakes in each RHIC ring. The polarization direction for each bunch was selected at the polarized H^- source, and each RHIC ring was loaded with 55 bunches each with a selected spin direction, spaced 212 nsec apart and with 5 consecutive missing bunches, used to abort the beams (the abort gap). Each RHIC store was typically six hours. The bunch length was $\sim$1.5 nsec and transverse size was $\sim$3 mm at 24 GeV/c and $\sim$1 mm at 100 GeV/c. The bunch polarizations for each RHIC fill were cycled through four preset spin patterns. The polarization direction of the beam for each scattering event was tagged using a RHIC timing clock. The timing clock information was verified by comparing to the location of the abort gap.

The bunch-to-bunch polarization over the course of a store of the RHIC beam was monitored by the RHIC pC polarimeter [24] for every store. This polarimeter uses *proton-carbon* elastic scattering in the Coulomb Nuclear Interference region. By use of a solid carbon ribbon target, the RHIC pC polarimeter measures relative beam polarization within 10 seconds of data-taking time. Normally, polarization does not vary bunch to bunch beyond statistical uncertainties. The polarization decay over the course of a store was measured to be 1% loss/hour or less. The store-by-store polarization variation can be large (several %). Therefore we consider this effect for the A_{NN} results, which is discussed later.

For the $\sqrt{s} = 6.8$ GeV data set (RHIC injection energy), only the clockwise RHIC beam (as seen from above) was filled and four RHIC stores were used, for a total of 15.5 hours. For the $\sqrt{s} = 13.7$ GeV data set (the RHIC beam at 100 GeV/c), both RHIC rings were filled, and the counter-clockwise beam was steered to miss the H-jet target, giving only scattering using the clockwise RHIC beam. For about 40% the data set, the counterclockwise beam was "anti-cogged" and crossed the H-jet target shifted in phase from the clockwise beam by 106 nsec. This data set used 19 RHIC stores, of 86 hours.

B. H-jet target

The H-jet-target system consisted of three parts: the atomic beam source; the scattering chamber; and the Breit-Rabi polarimeter. Collisions between the target proton and the beam proton occur in the scattering chamber, where recoil spectrometers were mounted to the left and right of the beam on vacuum flanges, as shown in Figs. 1 and 2. The entire system was placed on a rail perpendicular to the RHIC-beam direction and could be moved along the rail by ± 10 mm, in order to adjust the H-jet target center to the RHIC-beam center. The atomic beam was electron polarized and focused by a system of permanent sextupole magnets [33,34]. Atomic hydrogen nuclear polarization was achieved using two high radio frequency (RF) transitions. The polarized atomic hydrogen beam crossed the RHIC beam from above, at the scattering chamber. The velocity of the atomic beam was 1562 ± 50 m/sec [35] and negligible with respect to the RHIC beam. The target holding field, which is noted $\vec{B}$ in Fig. 1, was generated by two sets of opposing Helmholtz coils, with each set of coils separated by a central iron ring. The central field strength was 0.12 T with uniformity of $\Delta\vec{B}/\vec{B} < 5 \times 10^{-3}$ within a central region defined by a 10 mm diameter $\times$40 mm long cylinder [36,37]. A calculation of the field strength along the recoil proton path to the detectors is displayed in Fig. 3. The recoil proton detectors sit at $\sim$78 cm from the H-jet

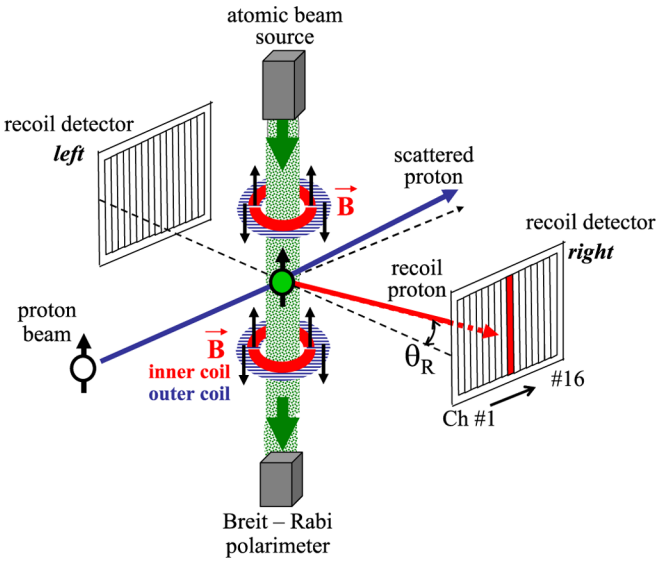

FIG. 1 (color online). Layout of the pp elastic scattering setup with an example of parallel proton spins, $p^{\uparrow}p^{\uparrow} \rightarrow pp$. The target protons cross the RHIC beam from above.

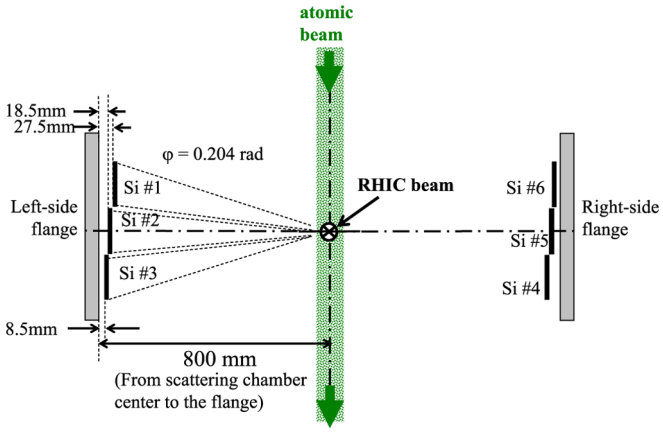

FIG. 2 (color online). Layout of the pp elastic scattering setup from the RHIC-beam view. The detectors were mounted on vacuum flanges on the scattering chamber and located to the left and right of the beam. Three pairs of silicon detectors covered an azimuthal angle of 11.7° centered on the horizontal midplane.

target center. The geometry of the yoke and coils as well as the excitations of the magnet coils were optimized to minimize the displacement of the recoil protons in the energy band of interest as they crossed the plane of the recoil detectors.

The Breit-Rabi polarimeter was below the RHIC beam, and determined the efficiency of the two RF transitions located upstream of the scattering chamber [37]. The Breit-Rabi polarimeter included a sextupole magnet system, two RF transitions, beam blockers, a beam chopper, and a commercial ion gauge biased with a low ripple power supply. The sextupole magnet system and two RF transitions in the Breit-Rabi polarimeter are the same type as those in the atomic beam source. The average efficiency of

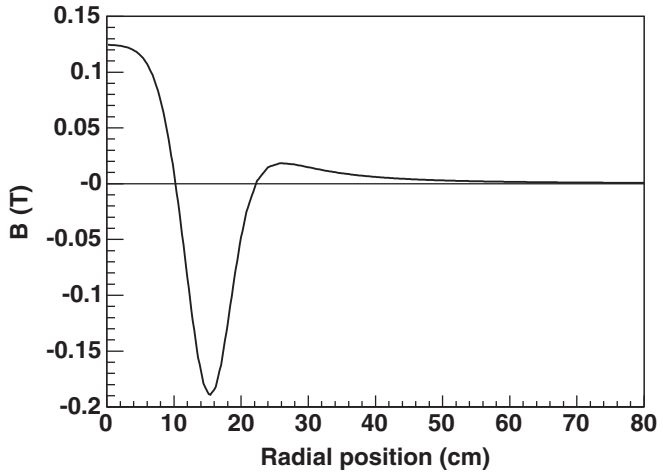

FIG. 3. The H-jet target holding magnetic field calculated by the OPERA program with the experimental setting: inner coil 349 A (N = 56); outer coil 275 A (N = 40). The recoil proton detectors sit at ~78 cm from the H-jet target center.

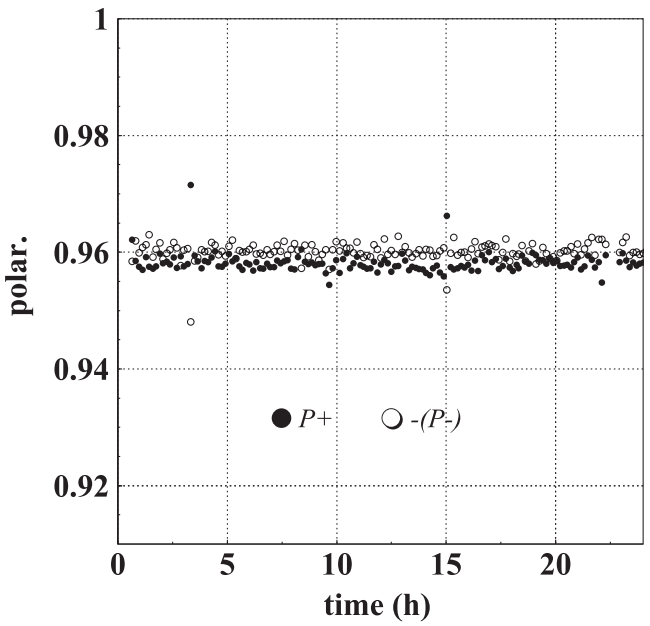

FIG. 4. Atomic hydrogen polarization measured by Breit-Rabi polarimeter.

the two RF transitions was 99.7% [35,36]. Figure 4 displays a sample of the measured $P_{\pm}$ in the 2004 run [35]. The polarization cycle was $(+/0/-) = (500/50/500)$ seconds, with the polarization selected by the on/off combination of two RF transitions; the strong field transition and the weak field transition. The mean value for nuclear polarization of the atoms was $|P_{\pm}| = 0.958$ [33,35,37]. The Breit-Rabi polarimeter measured the atomic hydrogen polarization; therefore we need to account for the effect on the polarization from background hydrogen molecules. The level of molecular hydrogen in the scattering chamber was measured to be $N(H_2)/N(H) \sim 0.015$ [34,36,38]. Assuming the molecular hydrogen to be unpolarized, this represents a 3% dilution of the atomic hydrogen polarization. The effective target polarization was $P_T = 0.924 \pm 0.018$, with the uncertainty dominated by the uncertainty in the molecular hydrogen fraction.

The transverse H-jet target size and atomic beam intensity for both spin states in the scattering chamber were measured with 2 mm and 11 mm diameter compression tubes [33]. At the center of the scattering chamber, the FWHM of the atomic beam was 5.5 mm. The atomic beam intensity was measured to be $(12.4 \pm 0.2) \times 10^{16}$ atoms/ sec [33–36,38].

Furthermore, we measured the target size by fixing the RHIC beam (FWHM ~ 2.4 mm) position and moving the entire H-jet-target system in 1.5 mm steps. In this method, the measured FWHM was 6.7 mm. The result is slightly wider than the expected value from the convolution of the RHIC-beam size and H-jet target size, 6 mm. Figure 5 displays event counts detected by the recoil spectrometer in the region of $0.6 < T_R < 7.2$ MeV versus position. The

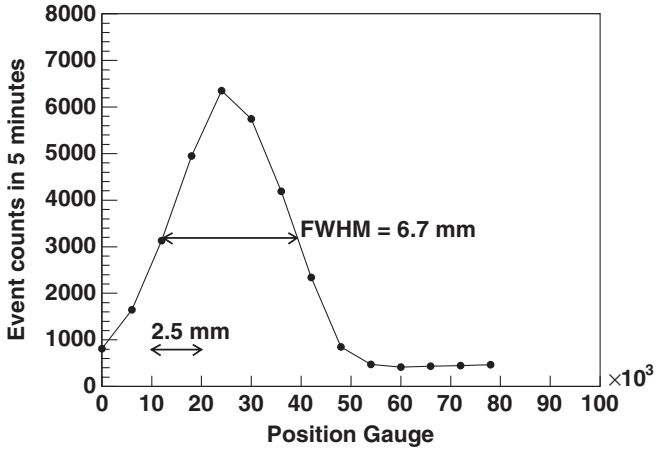

FIG. 5. Atomic beam profile measurements using the RHIC beam and the recoil spectrometer. This profile is obtained from event counts of the recoil protons in the region of $0.6 < T_R < 7.2$ MeV for five minutes/position. The tail of the distribution includes contributions from the calibration α sources, beam halo interactions, and scattering from the residual target gas.

background tail in Fig. 5 includes a lower energy tail from α particles from the calibration sources and beam halo interactions in addition to beam scattering from the residual target gas. The estimate of backgrounds is discussed later.

Taking the measured atomic beam intensity, velocity, and profile, the areal target thickness along the RHIC-beam axis was calculated to be $(1.3 \pm 0.2) \times 10^{12}$ atoms/cm^2 [35,38].

C. Recoil spectrometers

Recoil protons were detected using an array of silicon detectors. A schematic layout is shown in Figs. 1 and 2. The detectors were mounted on vacuum flanges on the scattering chamber and located to the left and right of the beam at a distance $D \sim 78$ cm from the H-jet target center. Three pairs of silicon detectors covered an azimuthal angle of 11.7° centered on the horizontal midplane. We employed two types of silicon detectors. Two out of three pairs of silicon detectors (Si#1, 4) and (Si#3, 6) were fabricated by Hamamatsu Photonics K.K., $\sim$385 μm thick and 70.4 mm (along the beam) $\times$50.0 mm (vertical) with a 4.4 mm read out pitch with 16 channels per detector. The other pair of silicon detectors (Si#2, 5) were fabricated by BNL Instrumentation Division, $\sim$414 μm thick and 70.0 mm (along the beam) $\times$64.0 mm (vertical) with a 4.38 mm read out pitch with 16 channels per detector.

Signals from each strip of 96 (= 16 strips/detector $\times$ 6 detectors) readout channels from the silicon detectors were shaped by a shaping amplifier and processed by a custom waveform digitizer (WFD). The WFD was a CAMAC module, hosting analog-to-digital converter (ADC) input channels with storage synchronous dynamic random access memory (SDRAM) and the CAMAC control circuitry. A trigger threshold was used to determine the presence of a significant signal in a particular bunch period, and if the signal was not detected, the ADC values were used for baseline calculations. The baseline for each signal was determined by averaging over 16 previous bunch periods with no significant signal. Waveforms were digitized at the equivalent frequency of 420 MHz (3 ADC channels per strip at 140 MHz) and analyzed by an on-board field programmable gate array (FPGA) chip, and the baseline subtraction was performed. These results provided online monitoring [39]. The event-by-event waveforms were recorded for offline analysis, digitized over the period between bunch crossing of 212 nsec.

Figure 6 displays time of flight (TOF) vs *deposit energy* scatter plot of 16 readout channels of one of the silicon detectors.

Each silicon detector covered elastic recoil angles corresponding to energy of $0.6 < T_R < 17.0$ MeV. The recoil angle, θ_R, was obtained by the detector channel number in $\simeq 5.5$ mrad steps. This angular resolution was comparable to the transverse H-jet target size. As we discussed in the previous section, the target holding field, in combination with the field return, has zero integrated field as seen by the recoil particles. The field effectively created a shift in the track of a half strip for particles of small kinetic energies ($T_R < 1$ MeV), in opposite directions for left and right scattering.

The (red) arrows in Fig. 6 indicate recoil protons. As we discuss in the next section, a correlation between energy and angle of recoil protons is observed. Recoil protons with T_R up to 7 MeV (up to channel #8) were fully absorbed. The vertical bands around 5 MeV in Fig. 6 are from the energy calibration α source ^{241}Am (5.486 MeV). In addition to ^{241}Am, three out of six silicon detectors (Si #4–6) calibrated by another α source ^{148}Gd (3.183 MeV). In this way, the energy calibration was performed using two α sources. We excluded events of these α source energies from physics analysis.

The resolution of T_R in the fully absorbed region was $\Delta T_R = 0.07$ MeV. More energetic protons punched through the detectors, depositing only a fraction of their energy (channel #9–16th). Therefore T_R for punch-through protons was corrected using the detector thickness and tables for energy loss in silicon [40]. There are two main contributions to the energy resolution of punch-through protons. (a) An uncertainty of the detector thickness $\sim$10 μm: This component becomes large as the recoil proton's kinetic energy is larger (deposit energy becomes small). (b) An uncertainty to judge, event by event, whether the proton deposited its full energy or punch-through. These cause a variation of the energy resolution. In the region of $5.7 < T_R < 7.2$ MeV, we accounted for (a) and (b) and obtained $\Delta T_R = 0.2$ MeV. In the region of $8.0 < T_R < 10.6$. MeV, $10.6 < T_R < 12$ MeV, and $14.5 < T_R < 17$ MeV, we accounted for (a) only. The energy

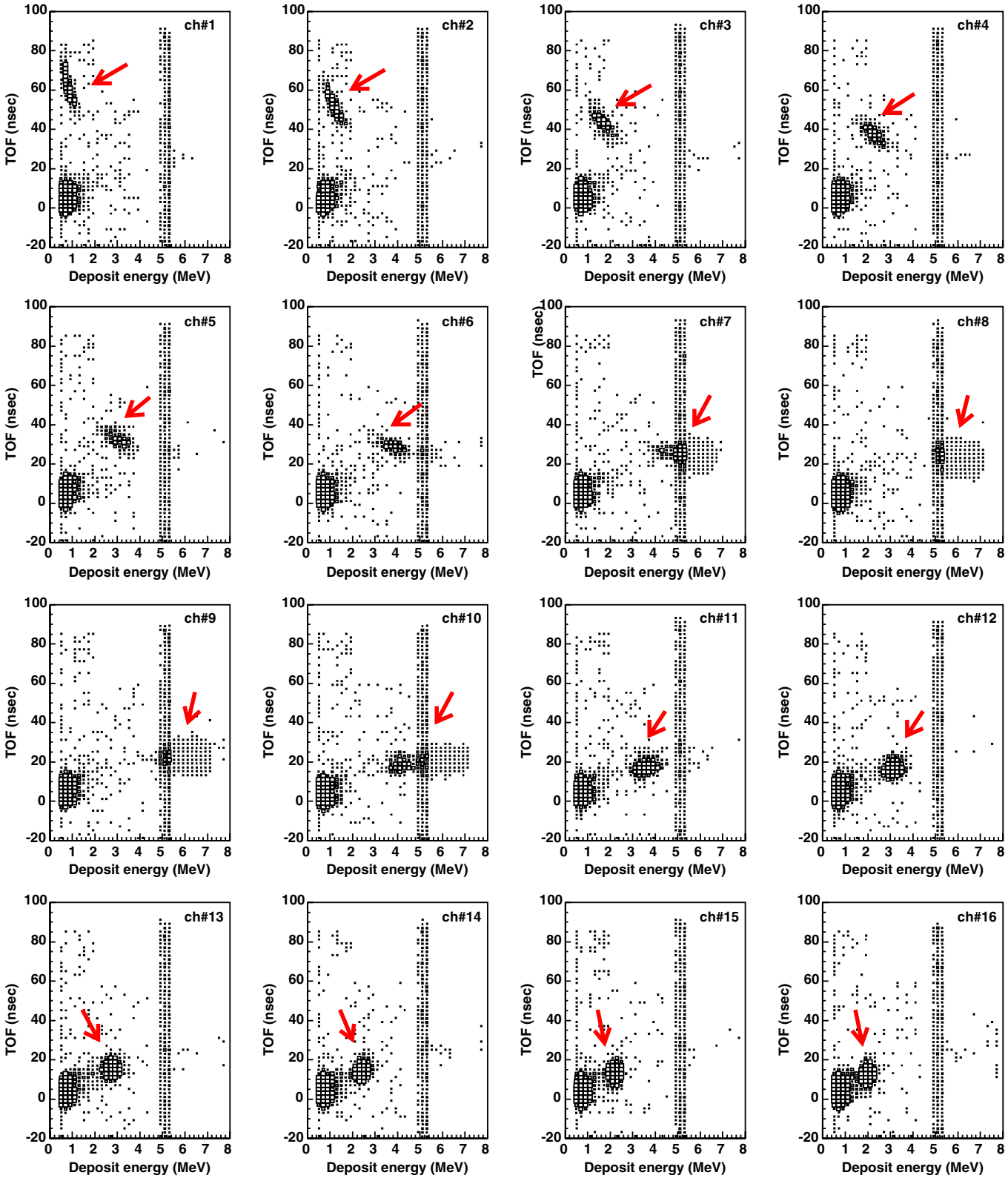

FIG. 6 (color online). TOF vs *deposit energy* scatter plot of one of the silicon detectors (Si #1) from ch#1 (left-upper plot) to ch#16 (right-bottom plot). The smaller channel number corresponds to the smaller θ_R. The (red) arrows indicate recoil protons. Events less than 2.5 MeV and less than 20 nsec are observed to be evenly distributed over the detector. These, which we call prompt particles, are possibly pions from beam-related interactions upstream. The vertical band just above 5 MeV deposit energy in each plot is populated with events from the energy calibration α source ^{241}Am (5.486 MeV). We have excluded data from this deposit energy range from this analysis.

resolutions were not the same but 0.1 MeV, 0.2 MeV, and 0.2 MeV, respectively. The 4-momentum transfer squared is given by $-t = 2M_p T_R$.

The TOF was measured with respect to the bunch arrival timed by the accelerator RF clock. The estimated TOF resolution was $\Delta\mathrm{TOF} \simeq 3$ nsec and was a convolution of the intrinsic time resolution of the detectors (≤ 2 nsec) and the length of the RHIC-beam bunches ($\sigma \simeq 1.5$ nsec). Details of the experimental setup for RUN4 were discussed in [32].

III. EVENT SELECTION

In the pp elastic scattering process, both the forward-scattered particle and the recoil particle are protons and no other particles are produced in the process. The elastic process can be identified by detecting the recoil particle only, by identifying the recoil particle as a proton through the relation of TOF and T_R, and by observing that the missing mass of the forward-scattered system is the proton mass. The procedure of elastic event selection is the same for both $\sqrt{s}$ energies. Details of elastic event selection were presented in [22,32] and we review the method here.

Recoil protons were identified using the nonrelativistic relation

$$T_R = \tfrac{1}{2} M_p (D/\mathrm{TOF})^2. \tag{11}$$

The upper plot of Fig. 7 displays TOF vs *deposit* energy scatter plot for all recorded events. The continuous band from deposit energy ~4 MeV and TOF ~ 20 nsec down to deposit energy ~0 MeV and TOF ~ 0 nsec is a mixture of "prompt and beam halo events" and "punch-through recoil protons." We used events down to deposit energy of 2 MeV for "punch-through protons." However, these events also included "prompt and beam halo" components. The upper plot of Fig. 8 displays deposit energy vs channel number ($\propto \theta_R$, $10 < \theta_R < 98$ mrad over the 16

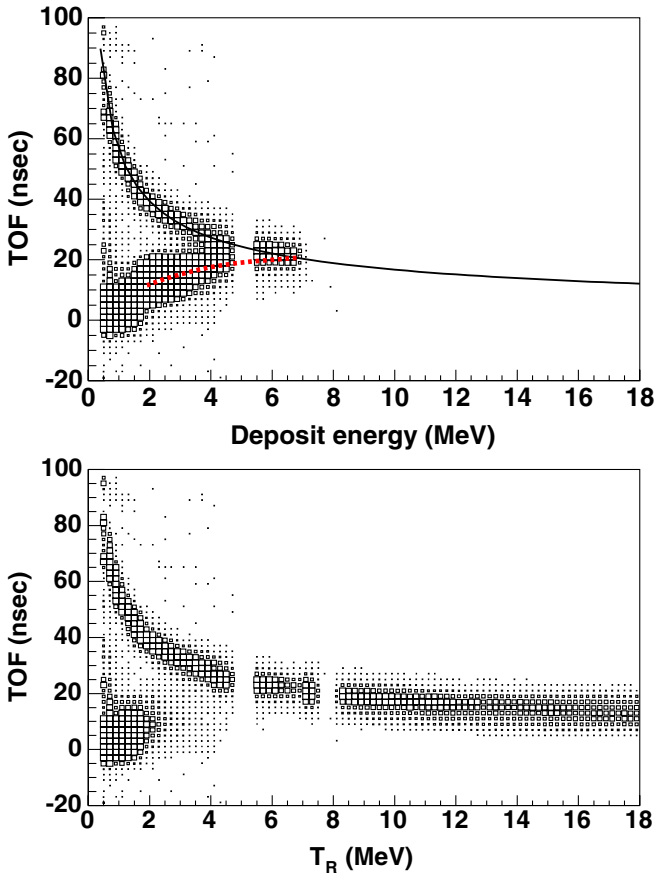

FIG. 7 (color online). Top: TOF vs *deposit* energy scatter plot for all recorded events. Detectors were ~400 μm thick and recoil protons with T_R up to 7 MeV were fully absorbed. More energetic protons punched through the detectors, depositing a fraction of their energy. The solid curve shows the kinematic function for protons. The dotted (red) curve shows the expected deposit energy for $T_R > 7$ MeV.

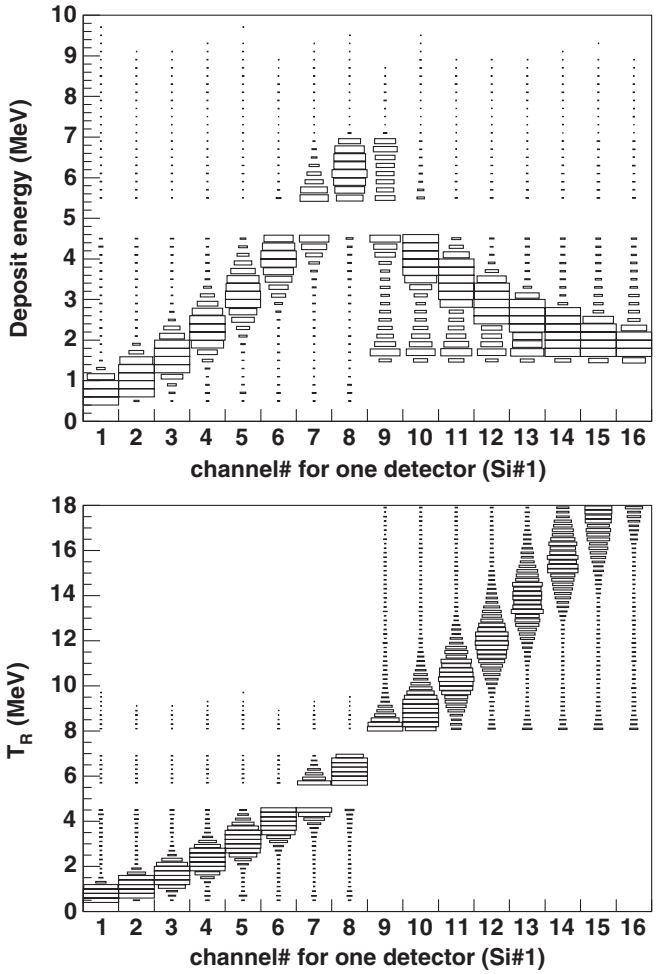

FIG. 8. Top: *Deposit* energy vs channel number scatter plot. A detector covers recoil angles of $10 < \theta_R < 98$ mrad. Events were selected in an expected TOF interval of ± 8 nsec around the solid line for $T_R < 7$ MeV and the (red) dotted line for $T_R \geq 7$ MeV in the upper plot of Fig. 7.

channels) scatter plot of one of the silicon detectors. From this plot, we decided to apply punch-through correction to the higher eight channels (#9–16th) for this detector. The corresponding angle for the boundary is $\theta_R \sim 54$ mrad. Because of detector alignment and the holding magnetic field, this boundary is not the same for all silicon detectors. The lower plot of Fig. 8 displays T_R vs channel number scatter plot. We applied punch-through correction for the #9–16th channels for this detector. The data set used for this plot is the same as the upper plot except for the events of deposit energy <2.0 MeV for the #9–16th channels. After punch-through correction, T_R of these events correspond to $T_R > 18$ MeV, which would be beyond the acceptance for elastics (beyond channel 16) for 3 out of 6 silicon detectors. Therefore, these events are not included in the lower plot of Fig. 8.

Finally, we display the T_R and TOF correlation in the lower plot of Fig. 7. The data sample is the same as the upper plot. We can see recoil protons clearly around the expected TOF value for T_R. Events less than 2.5 MeV and less than 20 nsec are prompt particles, which are possibly pions from beam-related interactions upstream. Events with more than 8 MeV and TOF less than 30 nsec are predominantly recoil protons, but prompt particles may also be there. Because we cannot separate between prompt events and recoil protons completely from TOF vs T_R correlation nor θ_R vs T_R correlation, we applied a background dilution correction to the measured raw asymmetry. By assuming (as observed) prompt events distribute equally over the detector, we estimated the component of prompt events to be less than 10% of all events after the selections. We also confirmed that prompt events show no asymmetry. The punch-through correction generated another corresponding *empty* vertical band around 8 MeV, which was populated by the calibration α source data and was removed from the plot (Fig. 7, bottom; Fig. 8, bottom). Events were selected in a TOF interval of ± 8 nsec around the expected TOF value for recoil protons of a given T_R.

On the basis of the measured θ_R and T_R, the mass of the undetected forward-scattered system (the missing mass M_X) can be reconstructed,

$$M_X{}^2 = M_p{}^2 - 2((M_p + E_1)T_R - \sin\theta_R |\vec{p}_1| \sqrt{2M_p T_R}), \tag{12}$$

where E_1 and $|\vec{p}_1|$ are the energy and momentum of the incident beam proton. For pp elastic scattering, events are identified on the basis of the θ_R-T_R relation

$$T_R = 2M_p \sin^2\theta_R \frac{E_1 - M_p}{E_1 + M_p}, \tag{13}$$

which is obtained applying $M_X = M_p$ in (12). For the two beam energies reported here, the difference in θ_R is $\sim$3 mrad at $T_R = 17$ MeV and smaller at lower T_R.

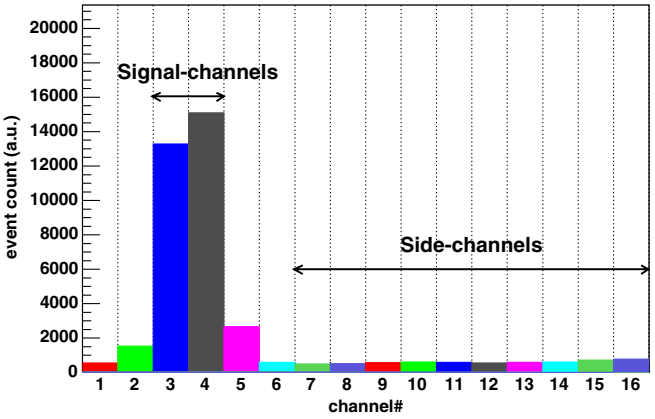

FIG. 9 (color online). Event distribution for the $1.4 < T_R < 1.8$ MeV interval as a function of channel number from the $\sqrt{s} = 13.7$ GeV data sample for one detector (Si #1). A detector covers recoil angles of $10 < \theta_R < 98$ mrad. For each T_R bin pp elastic events were selected in strips centered around the expected θ_R angle.

Figure 9 displays the event distribution of a certain T_R interval as a function of channel number. For each T_R bin pp elastic events were selected in strips centered around the expected θ_R angle.

Figures 10 and 11 display M_X^2 spectra with kinetic energy $0.6 < T_R < 1.4$ MeV and $8.0 < T_R < 12.0$ MeV at $\sqrt{s} = 6.8$ GeV and 13.7 GeV. The filled area corresponds to the events from selected strips centered around the expected θ_R angle. These data were selected for recoil protons, as discussed above. The width of the M_X^2 spectrum is expected to broaden as T_R and/or $|\vec{p}_1|$ increase:

$$\sigma_{M_X^2} \approx 2|\vec{p}_1| \sqrt{2M_p T_R} \Delta\theta_R \tag{14}$$

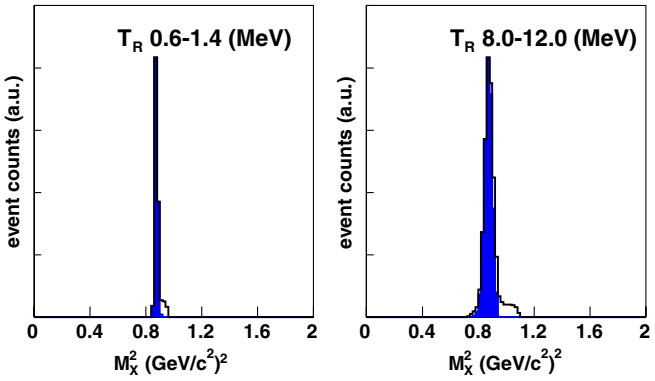

FIG. 10 (color online). M_X^2 spectra with $0.6 < T_R < 1.4$ MeV and $8.0 < T_R < 12$ MeV intervals for the $\sqrt{s} = 6.8$ GeV data set. The filled area corresponds to the events from selected strips centered around the expected θ_R angle. As T_R increases, the width of the M_X^2 spectrum broadens as (14).

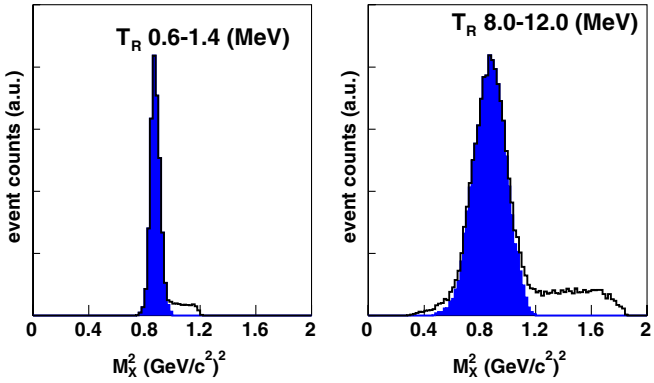

FIG. 11 (color online). M_X^2 spectra with $0.6 < T_R < 1.4$ MeV and $8.0 < T_R < 12$ MeV intervals for the $\sqrt{s} = 13.7$ GeV data set. The filled area corresponds to the events from selected strips centered around the expected θ_R angle. Compared to Fig. 10, the width of the M_X^2 spectrum also broadens as $|\vec{p}_1|$ increases as (14).

and is consistent with each spectrum in the figures. For example, the expected width of M_X^2 at $T_R = 10$ MeV, $|\vec{p}_1| = 100$ GeV/c is $\sigma_{M_X^2} = 0.15$ (GeV/c)^2, given the angle resolution $\Delta\theta_R \cong 5.5$ mrad, and it is consistent with the spectrum in Fig. 11 (right side).

The channel for diffractive dissociation opens at $M_X > M_p + M_\pi = 1.08$ GeV/c^2. The kinematical boundary for $M_X = M_p + M_\pi$ is given by (12) and is out of the acceptance for $\sqrt{s} = 6.8$ GeV as displayed in the upper plot of Fig. 12. For $\sqrt{s} = 13.7$ GeV, the kinematical boundary for $M_X = M_p + M_\pi$ is inside the acceptance and is distinguishable between the elastic and inelastic processes using the T_R and θ_R correlation as displayed in the lower plot of Fig. 12. The difference between the recoil angle of the elastic process and inelastic processes, $\Delta\theta$, decreases as T_R increases and $\Delta\theta = 8.3$ mrad at $T_R = 15$ MeV. There is a possibility that inelastic events smear from beyond the kinetic boundary into the elastic region, due to limited resolution for angle and kinetic energy in the punch-through region, $T_R > 8$ MeV. In order to estimate this contribution, we checked event distributions for higher recoil angles in lower T_R regions. For example, in Fig. 9, the kinetic boundary for inelastic processes corresponds to channel #9 and greater. The event distribution of channels #7–16, which are both inside and outside of the boundary, was flat and, therefore, the contribution from inelastic events was small. The inelastic contamination is estimated to be less than 0.5% for $T_R > 8$ MeV.

The selected event yield was accumulated over the entire experimental period and sorted by T_R bins. We collected 4.3 M events in 14 T_R bins at $\sqrt{s} = 13.7$ GeV and 0.8 M events in nine T_R bins at $\sqrt{s} = 6.8$ GeV in the region $0.6 < T_R < 17$ MeV $(0.001 < -t < 0.035$ (GeV/c)^2). Furthermore, the selected event yield in each T_R bin is sorted by spin states (beam, target, up-down) and the detector side (left-right). There are eight event yields for each T_R bin,

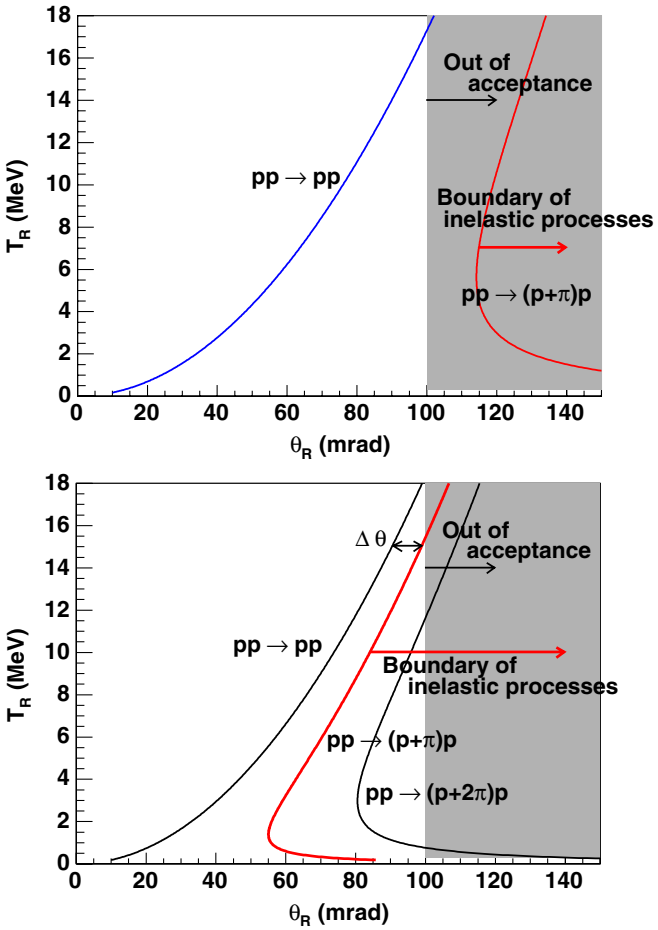

FIG. 12 (color online). Top: Calculation of T_R-θ_R correlation for $pp \to pp$ and inelastic process at $\sqrt{s} = 6.8$ GeV. Detectors cover $10 < \theta_R < 100$ mrad. Bottom: The same for $\sqrt{s} = 13.7$ GeV. The difference between the recoil angle of the elastic process and inelastic processes, $\Delta\theta$, decreases as T_R increases and $\Delta\theta = 8.3$ mrad at $T_R = 15$ MeV.

which are written in terms of A_N and A_{NN} below:

$$
\begin{aligned}
N^L_{\uparrow\uparrow} &= N_0 d\Omega_L L_{\uparrow\uparrow}\{1 - A_N(P^\uparrow_B - P^\uparrow_T) + A_{NN}P^\uparrow_B P^\uparrow_T\},\\
N^L_{\uparrow\downarrow} &= N_0 d\Omega_L L_{\uparrow\downarrow}\{1 - A_N(P^\uparrow_B + P^\downarrow_T) - A_{NN}P^\uparrow_B P^\downarrow_T\},\\
N^L_{\downarrow\uparrow} &= N_0 d\Omega_L L_{\downarrow\uparrow}\{1 - A_N(-P^\downarrow_B - P^\uparrow_T) - A_{NN}P^\downarrow_B P^\uparrow_T\},\\
N^L_{\downarrow\downarrow} &= N_0 d\Omega_L L_{\downarrow\downarrow}\{1 - A_N(-P^\uparrow_B + P^\uparrow_T) + A_{NN}P^\uparrow_B P^\uparrow_T\}
\end{aligned}
\tag{15}
$$

for the left side and

$$
\begin{aligned}
N^R_{\uparrow\uparrow} &= N_0 d\Omega_R L_{\uparrow\uparrow}\{1 + A_N(P^\uparrow_B - P^\uparrow_T) + A_{NN}P^\uparrow_B P^\uparrow_T\},\\
N^R_{\uparrow\downarrow} &= N_0 d\Omega_R L_{\uparrow\downarrow}\{1 + A_N(P^\uparrow_B + P^\downarrow_T) - A_{NN}P^\uparrow_B P^\downarrow_T\},\\
N^R_{\downarrow\uparrow} &= N_0 d\Omega_R L_{\downarrow\uparrow}\{1 + A_N(-P^\downarrow_B - P^\uparrow_T) - A_{NN}P^\downarrow_B P^\uparrow_T\},\\
N^R_{\downarrow\downarrow} &= N_0 d\Omega_R L_{\downarrow\downarrow}\{1 + A_N(-P^\downarrow_B + P^\downarrow_T) + A_{NN}P^\downarrow_B P^\downarrow_T\}
\end{aligned}
\tag{16}
$$

for the right side. We define positive A_N for observing more *recoil* protons to the beam right with beam polarization up, i.e. more *forward* protons to beam left, as required by the Basel convention [18].

N_0 is the normalization, $d\Omega_L$ is the detector acceptance for the left side, and $L_{\uparrow\uparrow}$ is the luminosity which is proportional to the product of beam and target intensities of both spin-up states. $P_B^{\uparrow}(>0)$ and $P_B^{\downarrow}(>0)$ are values of beam polarization up and down states and $P_B^{\uparrow} + P_B^{\downarrow} \equiv 2P_B$. (Similarly, $P_T^{\uparrow}(>0)$ and $P_T^{\downarrow}(>0)$ are values of target polarization up and down states and $P_T^{\uparrow} + P_T^{\downarrow} \equiv 2P_T$.) $N_{\uparrow\downarrow}^L$ is the number of *recoil* protons of selected pp elastic scattering events detected on the left of the beam for beam polarization up and target polarization down. Since P_T was stable over the entire run to $<1\%$, we use, for the A_{NN} measurement, $P_B P_T = P_T\langle P_B\rangle$, where $\langle P_B\rangle$ is averaged, weighted by the number of events, over the run.

IV. RESULTS

A. A_N at $\sqrt{s} = 6.8$ GeV

A_N data are obtained from the geometrical means of **target**-spin sorted event yields [41]:

$$A_N \cong \frac{1}{P_T}\frac{\sqrt{N_{0\uparrow}^L \cdot N_{0\downarrow}^R} - \sqrt{N_{0\uparrow}^R \cdot N_{0\downarrow}^L}}{\sqrt{N_{0\uparrow}^L \cdot N_{0\downarrow}^R} + \sqrt{N_{0\uparrow}^R \cdot N_{0\downarrow}^L}} \equiv \frac{\epsilon_T}{P_T}, \qquad (17)$$

where $N_{0\uparrow}^L (= N_{\uparrow\uparrow}^L + N_{\downarrow\uparrow}^L)$ is the number of *recoil* protons for selected pp elastic scattering events detected on the left of the beam with the direction of the target polarization up. The sum over beam polarization states results in an unpolarized beam at a level of $\leq 1/55 (= |P_B^{\uparrow} - P_B^{\downarrow}|/2P_B \equiv \epsilon_{P_B})$ of the beam polarization. As we mentioned already, the RHIC beam had 55 bunches (in 2004) with alternating spin patterns. By accumulating all stores, the value should be less than this. (Similarly averaging over the target polarization states results in an unpolarized target at a level of $\leq 0.2\% (= |P_T^{\uparrow} - P_T^{\downarrow}|/2P_T \equiv \epsilon_{P_T})$ of the target polarization.) The expression cancels luminosity and acceptance asymmetries. Equation (17) also defines the raw asymmetry, ϵ_T, related to the target polarization.

The backgrounds for the measurement of ϵ_T were from (a) a lower energy tail from alpha particles from the calibration sources; (b) events from the halo of the beam scattering from apertures upstream of the target (beam scraping); (c) elastic scattering of the proton beam from unpolarized residual target gas (unfocused molecular hydrogen); (d) inelastic scattering of the beam from the target gas (both atomic and molecular hydrogen); (e) prompt inelastic events that appear at early flight times and have typically lower deposited energy. We now discuss each background and obtain corrections and systematic uncertainties on the ϵ_T measurement.

Background (a) from the alpha sources was estimated from data taken with both beam and target off. The background was at a constant level in all strips and time-of-flight bin, but varied depending on deposited energy bin. The level corresponded to $r_\alpha =$ (number of source events)/(number of elastic events) $=$ 0.02 (for $T_R = 0.6$ to12 MeV) to $r_\alpha = 0.01$ (for $T_R = 14.5$ to 17 MeV). The background (b) from beam scraping was measured using beam on, target off data, and it was at a constant level in all strips, but varied depending on deposited energy bin, and time of flight. The background was $r_{\text{beam}} =$ (number of beam scraping events)/(number of elastic events) < 0.01 (for $T_R = 0.06$ to 12 MeV) to 0.01 ($T_R = 14.5$ to 17 MeV). Both backgrounds (a) and (b) were independent of the target polarization and dilute the ϵ_T signal. The measured ϵ_T was corrected for the dilution using $\epsilon_T = \epsilon_T(\text{measured}) \times (1 + r_\alpha + r_{\text{beam}})$. We have assigned a systematic uncertainty on this correction of $\pm 0.05\times (r_\alpha + r_{\text{beam}})$, based on the statistical uncertainties of the background measurements.

The background contribution (c) from the beam scattering elastically from the residual target gas (unpolarized molecular hydrogen) dilutes the target polarization by 3%. This was discussed in the target section and is included in the effective target polarization value and target polarization systematic error. This residual gas results in beam scattering upstream and downstream of the core of the target. When a deposited energy range is selected, this elastic scattering illuminates strips upstream and downstream of the signal strips, for example, as seen in Fig. 9. The events in the side channel strips include these elastics and backgrounds (a) and (b).

The background contribution (d), due to inelastic scattering of the beam from the target gas, where a recoil proton is observed through the $T_R -$ TOF correlation, is in general measured to be small, as discussed earlier. However, in the punch-through region, at larger $|t|$, there is also a background (e) from prompt inelastic events which appear to be recoil pions which deposit a small amount of energy and have a short time of flight. This can be seen in Fig. 7, where the prompt events appear in the lower left corner. We estimate a systematic uncertainty on ϵ_T from the prompt background of $\pm 10\%$ for ($T_R = 10 -$ 12 MeV) and $\pm 20\%$ for ($T_R = 14.5 - 17$ MeV), based on the missing mass distributions for these bins, where a broader distribution is observed, in addition to a flat background. We do not apply a correction, since we cannot measure this background directly. There is also a possible correlation with the target polarization for these events. The systematic uncertainty accounts for a prompt background with an analyzing power of the same magnitude as the elastic analyzing power.

We have also checked the consistency of these background estimates with the event distributions measured

TABLE I. Breakdown list of systematic uncertainty of A_N for $\sqrt{s} = 6.8$ GeV as a function of $-t$ in 9 T_R bins. There are five possible origins of systematic uncertainty from background: (a) calibration α sources; (b) beam scraping; (c) unpolarized residual target gas; (d) inelastic scattering events; (e) prompt inelastic events (see more details of each item in the text). Because (c) is included in the target polarization systematic error and (d) is small, we list items (a), (b), and (e). The total systematic uncertainty is the quadratic sum of (a), (b), and (e).

T_R (MeV)	$-\langle t\rangle$ (GeV/c)^2	$\Delta A_N(\text{sys}) \times 10^{-3}$ (a) $\pm$ (b) $\pm$ (e)	$\Delta A_N(\text{sys}) \times 10^{-3}$ total
0.6–1.2	0.0016	$1.4 \pm 0.5 \pm <0.1$	1.5
1.2–1.8	0.0028	$0.7 \pm 0.3 \pm <0.1$	0.8
1.8–2.5	0.0041	$0.9 \pm 0.5 \pm <0.1$	1.0
3.0–4.0	0.0066	$1.3 \pm 0.7 \pm <0.1$	1.5
4.0–4.7	0.0083	$1.1 \pm 0.7 \pm <0.1$	1.3
5.7–7.2	0.0120	$0.5 \pm 0.2 \pm <0.1$	0.5
8.0–10.0	0.0171	$1.6 \pm 0.6 \pm <0.1$	1.7
10.0–12.0	0.0207	$1.0 \pm 0.5 \pm 3.1$	3.3
14.5–17.0	0.0295	$0.6 \pm 0.6 \pm 8.0$	8.0

when the target was displaced so that the beam passed through the target tail (gauge position $60 - 78 \times 10^3$ in Fig. 5). The sum of the estimated backgrounds are consistent with the side channel measurements and displaced target measurements for the energy bins where the proton energy is fully absorbed, but for $8 < T_R < 16$ MeV and $T_R \geq 16$ MeV, an excess of background for the displaced target data of about 10%–15% and 20%, respectively, of itself was observed, which we have assigned as a systematic uncertainty for these bins.

In addition to these systematic uncertainties from backgrounds, the region of deposited energy from $T_R = 5.7$ to 7.2 MeV contains mixed events, with both stopped protons and punch-through protons. This creates a larger uncertainty for the proton energy, with a larger window for elastics and a larger background fraction. The bin also has a larger resolution for the recoil energy T_R; however, we have not assigned a systematic uncertainty for this, since the $-t$ dependence of ϵ_T is relatively flat in this region.

Table I gives the contributions to the systematic uncertainties for each bin. These uncertainties are independent, and the total uncertainty is their quadratic sum. The uncertainty on the target polarization, P_T in (17), $\Delta P_T/P_T = 2.0\%$, was presented earlier and is an overall normalization uncertainty for A_N.

Table II and Fig. 13 present the results for A_N, for $\sqrt{s} = 6.8$ GeV. The table presents the statistical uncertainties and bin-dependent systematic uncertainties which have been added in quadrature (the uncertainties are largely uncorrelated). In Fig. 13, the statistical uncertainties are shown with the points, the bin-dependent systematic uncertainties are shown as a band below the data, and the overall target polarization uncertainty is not shown.

TABLE II. A_N for $\sqrt{s} = 6.8$ GeV as a function of $-t$ in 9 T_R bins. The first uncertainty is statistical, followed by the systematic uncertainty from ϵ_T. The normalization uncertainty from the target polarization P_T is $\pm 2.0\% \times A_N$.

T_R (MeV)	$-\langle t\rangle$ (GeV/c)^2	A_N	$\Delta A_N \times 10^{-3}$ (stat. $\pm$ sys.)
0.6–1.2	0.0016	0.0369	3.5 ± 1.5
1.2–1.8	0.0028	0.0472	4.2 ± 0.8
1.8–2.5	0.0041	0.0409	4.2 ± 1.0
3.0–4.0	0.0066	0.0403	4.1 ± 1.5
4.0–4.7	0.0083	0.0421	4.6 ± 1.3
5.7–7.2	0.0120	0.0378	3.7 ± 0.5
8.0–10.0	0.0171	0.0366	4.1 ± 1.7
10.0–12.0	0.0207	0.0311	4.1 ± 3.3
14.5–17.0	0.0295	0.0398	4.5 ± 8.0

The solid curve in Fig. 13 is the QED prediction with no spin-dependent hadronic contribution, corresponding to the first term in (8). Parameters used for the first term are shown later in (19).

The A_N data at $\sqrt{s} = 6.8$ GeV are *not* consistent with the solid line ($\chi^2/\text{ndf} = 34.9/9$) and this discrepancy implies the presence of a hadronic spin-flip contribution, $\phi_5^{\text{had}}(s, t)$. We use the relative amplitude r_5 to quantify the spin-dependent contribution from the hadronic amplitude $\phi_5^{\text{had}}(s, t)$, which is defined as

$$r_5 = \frac{M_p \phi_5^{\text{had}}(s, t)}{\sqrt{-t}\,\text{Im}\,\phi_+^{\text{had}}(s, t)}. \tag{18}$$

The factor involving $1/\sqrt{-t}$ reflects the requirement that

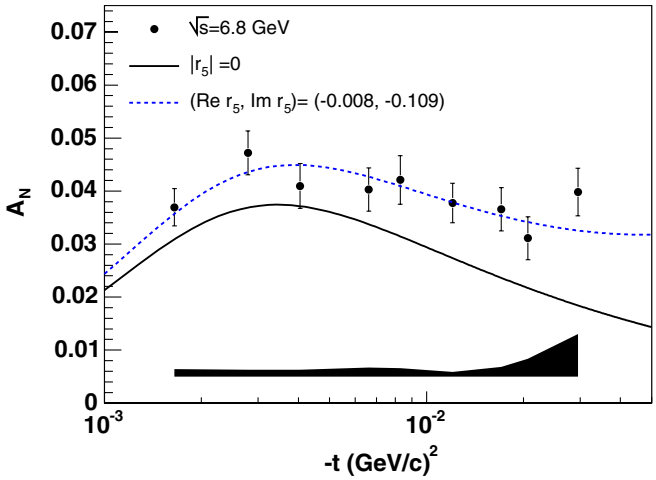

FIG. 13 (color online). A_N as a function of $-t$ for $pp^{\uparrow} \to pp$ at $\sqrt{s} = 6.8$ GeV. The uncertainties shown are statistical. The lower band represents the systematic uncertainty from ϵ_T. The solid curve corresponds to the prediction for no hadronic spin-flip contribution at $\sqrt{s} = 6.8$ GeV. The dashed curve is a fit to the data allowing for a hadronic spin-flip contribution to A_N ($\chi^2/\text{ndf} = 3.0/7$).

$\phi_5^{\rm had}(s,t) \propto \sqrt{-t}$ as $-t \to 0$, as a consequence of angular momentum conservation, as discussed earlier (1). r_5 is assumed to be complex and to vary with $\sqrt{s}$. But its variation in the $-t$ range of this experiment is usually neglected [7]. Using r_5, (8) is rewritten as

$$\frac{M_p A_N}{\sqrt{-t}}\frac{16\pi}{\sigma_{\rm tot}^2}\frac{d\sigma}{dt}e^{-Bt} = [\kappa(1-\rho\delta_C) - 2(\mathrm{Im}\, r_5 - \delta_C\, \mathrm{Re} r_5)]\frac{t_c}{t} - 2\,\mathrm{Re}\, r_5 + 2\rho\,\mathrm{Im}\, r_5, \quad (19)$$

and

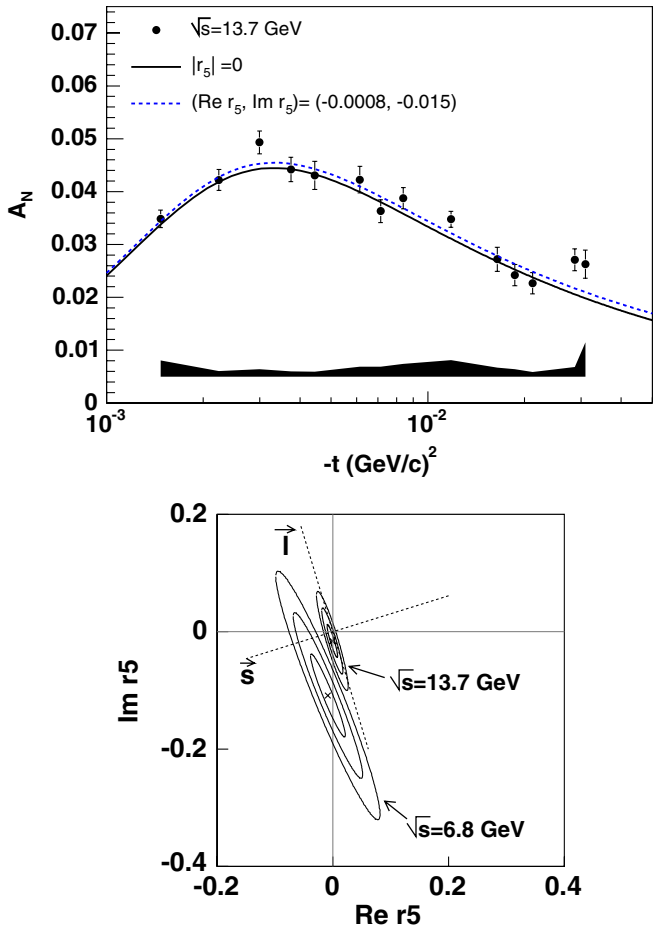

FIG. 14 (color online). Top: The results for A_N at $\sqrt{s} = 13.7$ GeV. The uncertainty shown is statistical. The lower band represents the total systematic uncertainties. The solid curve is the QED prediction with no spin-dependent hadronic contribution, is corresponding to the first term in (8) and (19) with $r_5 \equiv 0$. Parameters used here are $\sigma_{\rm tot} = 38.4$ mb [42], and $\rho = -0.08$ [42] at $\sqrt{s} = 13.7$ GeV. The value of $B = 12$ (GeV/c)^2 is obtained from the Refs. [43]. Bottom: Associated 1-σ, 2-σ, and 3-σ contours at $\sqrt{s} = 6.8$ GeV (lower) and $\sqrt{s} = 13.7$ GeV. The axes indicated as dashed lines are a rotated coordinate system along the major ($\vec{l}$) and minor ($\vec{s}$) axis of the error ellipses for $\sqrt{s} = 13.7$ GeV, determined empirically.

$$\frac{16\pi}{\sigma_{\rm tot}^2}\frac{d\sigma}{dt}e^{-Bt} = \left(\frac{t_c}{t}\right)^2 - 2(\rho+\delta_C)\frac{t_c}{t} + (1+\rho^2), \quad (20)$$

where $t_c \cong 8\pi\alpha/\sigma_{\rm tot}$. Parameters used here are the total cross section $\sigma_{\rm tot} = 38.4$ mb [42] and the real to imaginary ratio of non-spin-flip hadronic amplitudes $\rho = -0.25$ [42] at $\sqrt{s} = 6.8$ GeV. The value of $B = 11$ (GeV/c)^2 is obtained from the Refs. [43]. The solid curve in Fig. 13, which is the QED prediction with no spin-dependent hadronic contribution, corresponds to the first term in (8) and (19) with $r_5 \equiv 0$. Applying r_5 as a free parameter, we obtain the fit to the A_N data shown as the dashed line in Fig. 13, with $\chi^2/\mathrm{ndf} = 3.0/7$.

On the other hand, as we have previously reported [22], the A_N data at $\sqrt{s} = 13.7$ GeV are consistent with the QED prediction ($\chi^2/\mathrm{ndf} = 13.4/14$). The upper plot of Fig. 14 displays the results for A_N at $\sqrt{s} = 13.7$ GeV.

The r_5 value obtained from the fit for $\sqrt{s} = 6.8$ GeV is $(\mathrm{Re}\, r_5, \mathrm{Im}\, r_5) = (-0.008, -0.109)$ with strongly correlated uncertainties. The associated contours of 1-σ, 2-σ, and 3-σ for r_5 at $\sqrt{s} = 6.8$ and 13.7 GeV are displayed in the lower plot of Fig. 14. To remove the correlation between Re r_5 and Im r_5 due to the combined contributions to the amplitude and shape of A_N from (Re r_5, Im r_5) (19), we introduce a rotated coordinate system along the major ($\vec{l}$) and minor ($\vec{s}$) axes of the error ellipses for $\sqrt{s} = 13.7$ GeV, determined empirically. These axes are indicated as dashed lines on the lower panel of Fig. 14, for $\sqrt{s} = 13.7$ GeV, are $\vec{l} = (0.293 \cdot \mathrm{Re}\vec{r}_5 - 0.956 \cdot \mathrm{Im}\vec{r}_5)$ and $\vec{s} = (0.956 \cdot \mathrm{Re}\vec{r}_5 + 0.293 \cdot \mathrm{Im}\vec{r}_5)$. The 1-$\sigma$ fit results along these axes are $(\mathrm{l};\mathrm{s}) = (0.014 \pm 0.029; 0.005 \pm 0.003)$, with the errors now uncorrelated. Similarly, for $\sqrt{s} = 6.8$ GeV, $\vec{l} = (0.375 \cdot \mathrm{Re}\vec{r}_5 - 0.927 \cdot \mathrm{Im}\vec{r}_5)$ and $\vec{s} = (0.927 \cdot \mathrm{Re}\vec{r}_5 + 0.375 \cdot \mathrm{Im}\vec{r}_5)$, with 1-$\sigma$ fit results $(\mathrm{l};\mathrm{s}) = (0.098 \pm 0.076; 0.046 \pm 0.008)$.

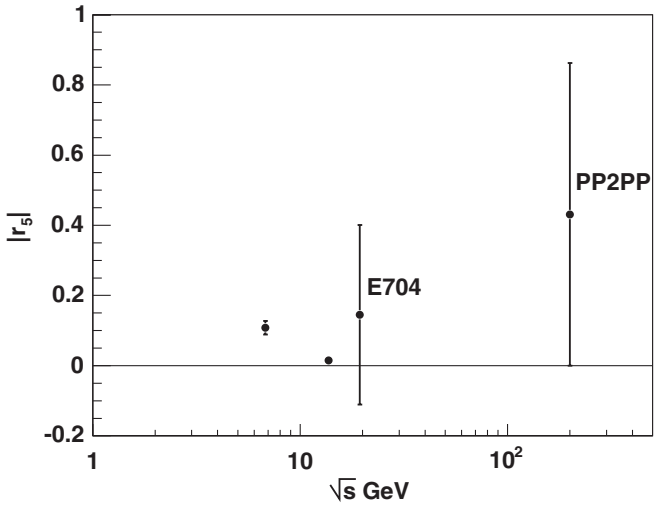

FIG. 15. Measurements of the absolute value of the hadronic spin-flip amplitude $|r_5|$ as a function of $\sqrt{s}$.

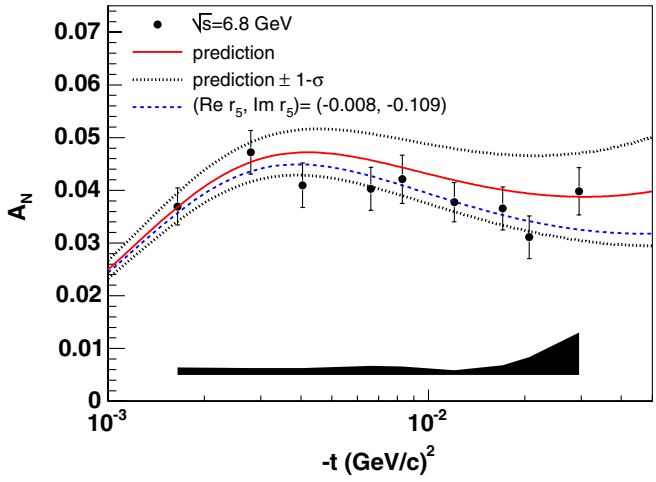

FIG. 16 (color online). A theoretical prediction for A_N at $\sqrt{s} = 6.8$ GeV [15] using parameters based on *proton-carbon* elastic scattering data and the previously published result for *proton-proton* at $\sqrt{s} = 13.7$ GeV. Dotted lines are 1-σ theoretical uncertainties. Data points from this experiment are also shown for comparison, along with the fit to the data (dashed line).

Figure 15 indicates the magnitude of $|r_5|$ as a function of $\sqrt{s}$. The uncertainties shown for $|r_5|$ reflect the uncertainty contours in the (Re r_5, Im r_5) plane (see e.g. bottom plot of Fig. 14). From this figure, the result for $\sqrt{s} = 6.8$ GeV is incompatible with no hadronic single spin-flip at a 5.8-σ level, while the result for r_5 for $\sqrt{s} = 13.7$ GeV is compatible with $r_5 = 0$ at a 1.6-σ level. These values for the previous measurements at $\sqrt{s} = 19.4$ GeV and 200 GeV are also displayed for comparison. The results for r_5 for $\sqrt{s} = 19.4$ GeV (E704) [20] and $\sqrt{s} = 200$ GeV (PP2PP) [21] are compatible with zero. These A_N results at different $\sqrt{s}$ energies may indicate a $\sqrt{s}$ dependence of r_5.

In Fig. 16 we present the results for A_N at $\sqrt{s} = 6.8$ GeV (as in Fig. 13), with the prediction from Ref. [15]. The prediction used A_N results from *proton-carbon* scattering [23,24] and from *proton-proton* scattering at $\sqrt{s} = 13.7$ GeV. The data are well described by this theoretical approach, which predicted the observed energy dependence of the hadronic single spin-flip amplitude.

B. A_{NN} at $\sqrt{s} = 6.8$ and 13.7 GeV

A_{NN}, which is defined in (9), can be determined from the spin sorted event yields [32]:

$$\begin{aligned} A_{NN} &\cong \frac{1}{P_T P_B}\left(\frac{1}{2}\frac{(N^L_{\uparrow\uparrow} + N^L_{\downarrow\downarrow}) - (N^L_{\uparrow\downarrow} + N^L_{\downarrow\uparrow})}{(N^L_{\uparrow\uparrow} + N^L_{\downarrow\downarrow}) + (N^L_{\uparrow\downarrow} + N^L_{\downarrow\uparrow})} + \frac{1}{2}\right. \\ &\quad \left. \times \frac{(N^R_{\uparrow\uparrow} + N^R_{\downarrow\downarrow}) - (N^R_{\uparrow\downarrow} + N^R_{\downarrow\uparrow})}{(N^R_{\uparrow\uparrow} + N^R_{\downarrow\downarrow}) + (N^R_{\uparrow\downarrow} + N^R_{\downarrow\uparrow})} - \epsilon_{L_B}\epsilon_{L_T}\right) \\ &\equiv \frac{1}{P_T P_B}(\epsilon_{NN} - \epsilon_{L_B}\epsilon_{L_T}). \end{aligned} \tag{21}$$

The approximation refers to dropping very small terms which include the difference in absolute polarization for up vs down polarization directions, for the beam and target. Equation (21) defines the raw *double*-spin asymmetry ϵ_{NN}.

P_B can be obtained from the raw asymmetry of *beam*-spin sorted event yields, ϵ_B, normalized by A_N:

$$P_B = \frac{\epsilon_B}{A_N}. \tag{22}$$

Because A_N for pp elastic scattering does not depend on the reference frame, we can change the role of which is polarized between a target proton and beam proton. Substituting (17), P_B is measured by our system as

$$P_B = -P_T\frac{\epsilon_B}{\epsilon_T}. \tag{23}$$

Therefore (21) is rewritten as

$$A_{NN} \cong -\frac{1}{P_T^2}\frac{\epsilon_T}{\epsilon_B}(\epsilon_{NN} - \epsilon_{L_B}\epsilon_{L_T}), \tag{24}$$

and this equation is used to obtain A_{NN}. In this way, we measured A_{NN} from three types of raw asymmetries, which were obtained by changing beam and target spin combinations only, and used the well-measured P_T. In this approach the common components of systematic uncertainty for ϵ_T and ϵ_B were minimized.

For A_{NN}, unlike A_N, the relative luminosity for the different spin orientations must be considered. The luminosity difference between spin-up and spin-down is defined as ϵ_{L_B} for beam spin and as ϵ_{L_T} for target spin:

$$\begin{aligned} \epsilon_{L_B} &= \frac{(L_{\uparrow\uparrow} + L_{\uparrow\downarrow}) - (L_{\downarrow\uparrow} + L_{\downarrow\downarrow})}{(L_{\uparrow\uparrow} + L_{\uparrow\downarrow}) + (L_{\downarrow\uparrow} + L_{\downarrow\downarrow})}, \\ \epsilon_{L_T} &= \frac{(L_{\uparrow\uparrow} + L_{\downarrow\uparrow}) - (L_{\uparrow\downarrow} + L_{\downarrow\downarrow})}{(L_{\uparrow\uparrow} + L_{\downarrow\uparrow}) + (L_{\uparrow\downarrow} + L_{\downarrow\downarrow})}, \end{aligned} \tag{25}$$

where the spin-dependent luminosity $L_{\uparrow\downarrow}$ is proportional to the product of beam intensity and target density for spin-up beam and spin-down target. The target spin was reversed every five minutes and its density for both spin states was constantly monitored with an ion gauge located below the beam at the end of the Breit-Rabi polarimeter. The density was stable during the data-taking period. On the other hand, the RHIC-beam intensity can vary for every bunch and RHIC store. The RHIC-beam bunch intensity was constantly monitored by wall current monitors [44]. However, the variations integrated over the experiment were small. We obtained $\epsilon_{L_T} \cdot \epsilon_{L_B} \sim 10^{-8}$ and neglect this term. Spin-dependent luminosities are also obtained from eight event yields which we have already introduced in (15) and (16). We estimated $\epsilon_{L_B} \cdot \epsilon_{L_T} = -0.0004 \pm 0.0001$ for $\sqrt{s} = 6.8$ GeV, and $\epsilon_{L_B} \cdot \epsilon_{L_T} = 0.0001 \pm 0.0001$ for $\sqrt{s} = 13.7$ GeV. These values, although not from an independent monitor, confirm the small contribution from this term. Therefore, the luminosity asymmetries

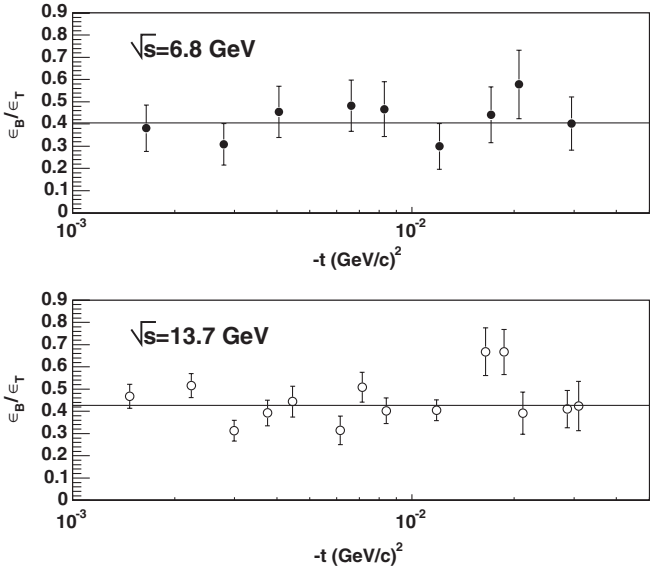

FIG. 17. Upper plot: ϵ_B/ϵ_T as a function of $-t$ at $\sqrt{s} = 6.8$ GeV with filled circles. The uncertainties shown are statistical. Bottom plot: the same for 13.7 GeV.

for both beam energies were quite small compared to the statistical uncertainty.

Figure 17 displays ϵ_B/ϵ_T as a function of $-t$ for $\sqrt{s} = 6.8$ GeV and $\sqrt{s} = 13.7$ GeV. The statistical uncertainty for ϵ_B/ϵ_T is equivalent to treating the uncertainties of the numerator and denominator as independent measurements. ϵ_B/ϵ_T should be independent of $-t$. Fit results for a constant value for the entire $-t$ range are 0.405 ± 0.038 ($\chi^2/\text{ndf} = 4.4/8$) for $\sqrt{s} = 6.8$ GeV and 0.426 ± 0.017 ($\chi^2/\text{ndf} = 25.4/13$) for $\sqrt{s} = 13.7$ GeV. Because of larger systematic uncertainties in the recoil punch-through region ($T_R > 4.7$ MeV), we use the peak A_N region of $1.0 < T_R < 4.7$ MeV and combine energy bins to determine ϵ_B/ϵ_T. We obtain $\langle \epsilon_B/\epsilon_T \rangle = 0.421 \pm 0.054$ for $\sqrt{s} = 6.8$ GeV and $\langle \epsilon_B/\epsilon_T \rangle = 0.415 \pm 0.022$ for $\sqrt{s} = 13.7$ GeV. (The average RHIC-beam polarization for the 2004 data-taking period is then obtained by $P_B = \langle \epsilon_B/\epsilon_T \rangle \times P_T$. $P_B = 0.389 \pm 0.050$ for $\sqrt{s} = 6.8$ GeV and $P_B = 0.383 \pm 0.020$ for $\sqrt{s} = 13.7$ GeV.) In order to study the effect of the fluctuations in ϵ_B/ϵ_T vs $-t$, we substituted ϵ_B/ϵ_T instead of $\langle \epsilon_B/\epsilon_T \rangle$ and compared A_{NN} between the two. The difference of each A_{NN} data points are the order of 10^{-3}. These differences are small compared to the statistical uncertainty of A_{NN} for both beam energies. Since P_T was stable over the entire run to $<1\%$, ϵ_T was stable. Then, $\langle \epsilon_B/\epsilon_T \rangle = \langle \epsilon_B \rangle/\epsilon_T$, and summing the events for the entire data set is identical to using the mean weighted by the event counts in each store. Consequently, the A_{NN} results accounted for the store-by-store variation of the RHIC-beam polarization. The systematic uncertainties in the measurement of A_{NN}, evaluated using (24), are in two categories: T_R bin dependent and the overall normalization. The ϵ_{NN} values are corrected for backgrounds from α particles from calibration sources and beam scraping. Spin-independent backgrounds cancel in the ratio ϵ_B/ϵ_T, specifically the backgrounds due to α particles from the sources. Background from beam scraping, at $<1\%$ of the elastic signal, is negligible. The uncertainty on target polarization gives normalization uncertainties of $\Delta P_T/P_T = 2.0\%$ for $\sqrt{s} = 6.8$ GeV and $\sqrt{s} = 13.7$ GeV. Inelastic scattering processes, discussed earlier, are negligible. The systematic uncertainties are summarized in Tables III and IV.

TABLE III. A_{NN} for $\sqrt{s} = 13.7$ GeV as a function of $-t$ in 14 T_R bins. The first uncertainty is statistical, followed by the systematic uncertainty. The normalization uncertainty from the target polarization P_T is $\pm 4.0\% \times A_{NN}$.

T_R (MeV)	$-\langle t \rangle$ (GeV$^2/c^2$)	A_{NN}	$\Delta A_{NN} \times 10^{-3}$ (stat. $\pm$ sys.)
0.6–1.0	0.0015	−0.0055	4.3 ± 1.3
1.0–1.4	0.0022	−0.0011	5.2 ± 3.4
1.4–1.8	0.0030	−0.0040	5.7 ± 1.5
1.8–2.2	0.0037	−0.0001	6.0 ± 1.4
2.2–2.5	0.0044	−0.0048	6.9 ± 1.7
3.0–3.5	0.0061	−0.0028	6.6 ± 0.1
3.5–4.2	0.0071	0.0059	5.6 ± 2.3
4.2–4.7	0.0084	−0.0095	5.2 ± 0.8
5.7–7.2	0.0118	−0.0021	3.9 ± 0.5
8.0–9.3	0.0165	−0.0052	6.2 ± 2.1
9.3–10.6	0.0187	0.0005	5.2 ± 1.2
10.6–12.0	0.0212	0.0006	5.2 ± 2.5
14.5–16.0	0.0287	−0.0030	5.4 ± 0.9
16.0–17.0	0.0309	−0.0013	6.9 ± 0.3

The upper plot of Fig. 18 displays the results for A_{NN} at $\sqrt{s} = 6.8$ GeV (filled circles) and 13.7 GeV (open circles). The uncertainties shown are statistical. The lower bands represent the systematic uncertainties (normalization uncertainties are not included). The χ^2/ndf values, comparing to a constant value of zero over the entire $-t$ region, are $17.1/9$ for $\sqrt{s} = 6.8$ GeV and $8.1/14$ for $\sqrt{s} = 13.7$ GeV.

TABLE IV. A_{NN} for $\sqrt{s} = 6.8$ GeV as a function of $-t$ in nine T_R bins. The first uncertainty is statistical, followed by the systematic uncertainty. The normalization uncertainty from the target polarization P_T is $\pm 4.0\% \times A_{NN}$.

T_R (MeV)	$-\langle t \rangle$ (GeV$/c)^2$	A_{NN}	$\Delta A_{NN} \times 10^{-3}$ (stat. $\pm$ sys.)
0.6–1.2	0.0017	−0.0285	9.0 ± 3.5
1.2–1.8	0.0028	0.0096	10.7 ± 3.8
1.8–2.5	0.0041	0.0027	10.8 ± 1.9
3.0–4.0	0.0066	0.0077	10.5 ± 1.3
4.0–4.7	0.0083	0.0230	11.8 ± 2.9
5.7–7.2	0.0120	0.0060	9.5 ± 3.1
8.0–10.0	0.0171	0.0119	10.5 ± 1.1
10.0–12.0	0.0207	−0.0127	10.4 ± 3.6
14.5–17.0	0.0295	0.0086	11.2 ± 2.0

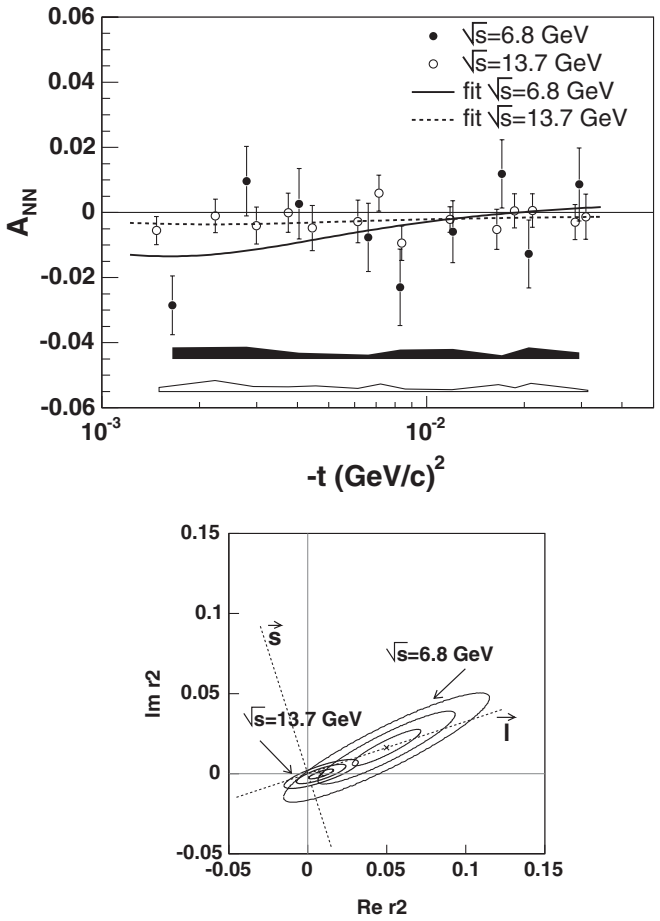

FIG. 18. Top: A_{NN} as a function of $-t$ for $p^{\uparrow}p^{\uparrow} \to pp$ at $\sqrt{s} = 6.8$ GeV with filled circles and 13.7 GeV with open circles. The uncertainties shown are statistical. The lower bands represent the systematic uncertainties. The solid line is a fitting result for $\sqrt{s} = 6.8$ GeV and the dashed line is for 13.7 GeV. Bottom: Associated 1-σ, 2-σ, and 3-σ contours at $\sqrt{s} = 6.8$ GeV and 13.7 GeV. The axes indicated as dashed lines are a rotated coordinate system along the major ($\vec{l}$) and minor ($\vec{s}$) axes of the error ellipses for $\sqrt{s} = 13.7$ GeV, determined empirically.

The mean values for A_{NN} for the region $0.001 < -t < 0.032$ $(\mathrm{GeV}/c)^2$ are $\langle A_{NN}\rangle = -0.005 \pm 0.003$ for $\sqrt{s} = 6.8$ GeV and $\langle A_{NN}\rangle = -0.002 \pm 0.002$ for $\sqrt{s} = 13.7$ GeV.

The relative amplitude r_2 is used to quantify the strength of the double spin-flip hadronic amplitude, $\phi_2^{\mathrm{had}}(s, t)$, relative to the non-spin-flip amplitude, $\phi_+^{\mathrm{had}}(s, t)$. This is defined as

$$r_2 = \frac{\phi_2^{\mathrm{had}}(s, t)}{2\,\mathrm{Im}\,\phi_+^{\mathrm{had}}(s, t)}. \tag{26}$$

In this parametrization, r_2 has no $-t$ dependence for $-t < 0.05$ $(\mathrm{GeV}/c)^2$ [3] and satisfies the requirement of angular momentum conservation. Using r_2 and r_5, (10) is rewritten as

$$A_{NN}\frac{d\sigma}{dt} = -\frac{2t}{m_p^2}((\mathrm{Im}\,r_5)^2 + (\mathrm{Re}\,r_5)^2) + 2\frac{t_c\kappa}{m_p^2}\,\mathrm{Re}\,r_5 + 2\,\mathrm{Re}\,r_2\left(\rho - \frac{t_c}{t}\right) + 2\,\mathrm{Im}\,r_2 - \frac{t_c\kappa^2}{2m_p^2}. \tag{27}$$

To obtain the r_2 value from the A_{NN} data, we applied a fit using (27) [45]. We set $\mathrm{Im}\,r_2$ and $\mathrm{Re}\,r_2$ as free parameters and fixed values for $\mathrm{Im}\,r_5$ and $\mathrm{Re}\,r_5$, obtained from the A_N data and (8) and (18): $(\mathrm{Re}\,r_5, \mathrm{Im}\,r_5) = (-0.008, -0.109)$ for $\sqrt{s} = 6.8$ GeV and $(\mathrm{Re}\,r_5, \mathrm{Im}\,r_5) = (-0.0008, -0.015)$ for $\sqrt{s} = 13.7$ GeV. The solid line in the top panel of Fig. 18 is the fit result for $\sqrt{s} = 6.8$ GeV with $\chi^2/\mathrm{ndf} = 12.9/7$; the dashed line is the fit result for 13.7 GeV with $\chi^2/\mathrm{ndf} = 5.2/12$. The r_2 value obtained is $(\mathrm{Re}\,r_2, \mathrm{Im}\,r_2) = (0.050, 0.016)$ for $\sqrt{s} = 6.8$ GeV, and $(\mathrm{Re}\,r_2, \mathrm{Im}\,r_2) = (0.008, 0.000)$ for $\sqrt{s} = 13.7$ GeV. The lower panel of Fig. 18 displays associated 1-σ, $2-\sigma$, and 3-σ contours at $\sqrt{s} = 6.8$ GeV and 13.7 GeV.

The solutions with no hadronic double spin-flip, $(\mathrm{Re}\,r_2, \mathrm{Im}\,r_2) = (0, 0)$ and fixed values for single spin-flip have $\chi^2/\mathrm{ndf} = 20.7/9$ for $\sqrt{s} = 6.8$ GeV and $8.9/14$ for $\sqrt{s} = 13.7$ GeV. This solution for $\sqrt{s} = 6.8$ GeV lies within the 3-σ uncertainty contour and the solution for $\sqrt{s} = 13.7$ GeV lies on a 2-σ contour.

To remove the correlation between $\mathrm{Re}\,r_2$ and $\mathrm{Im}\,r_2$ due to (27), we, again, introduce a rotated coordinate system along the major ($\vec{l}$) and minor ($\vec{s}$) axis of the error ellipses for $\sqrt{s} = 13.7$ GeV, determined empirically. These axes are indicated as dashed lines on the lower panel of Fig. 18, for $\sqrt{s} = 13.7$ GeV, with $\vec{l} = (0.951 \cdot \mathrm{Re}\,\vec{r_2} + 0.310 \cdot \mathrm{Im}\,\vec{r_2})$ and $\vec{s} = (-0.310 \cdot \mathrm{Re}\,\vec{r_2} + 0.951 \cdot \mathrm{Im}\,\vec{r_2})$. The fit results given along the rotated axes are $(\mathrm{l; s}) = (0.008 \pm 0.008; 0.003 \pm 0.002)$, with the errors now uncorrelated. Similarly, for $\sqrt{s} = 6.8$ GeV, $\vec{l} = (0.900 \cdot \mathrm{Re}\,\vec{r_2} + 0.438 \cdot \mathrm{Im}\,\vec{r_2})$, and $\vec{s} = (-0.438 \cdot \mathrm{Re}\,\vec{r_2} + 0.900 \cdot \mathrm{Im}\,\vec{r_2})$, with fit results $(\mathrm{l; s}) = (0.051 \pm 0.025; 0.007 \pm 0.004)$. At these energies, the double spin-flip amplitude $\phi_2^{\mathrm{had}}(s, t)$ is small but nonzero at a 2-σ level.

In past experiments, the imaginary part of $\phi_2^{\mathrm{had}}(s, t)$ at $|t| = 0$ was measured through the difference between the pp total cross sections for antiparallel and parallel initial spin states, $\Delta\sigma_T$. The relationship between $\Delta\sigma_T$ and $\mathrm{Im}\,\phi_2^{\mathrm{had}}(s, 0)$ is

$$\Delta\sigma_T = \sigma_{\uparrow\downarrow} - \sigma_{\uparrow\uparrow} = -\frac{8\pi}{\sqrt{s(s - 4M_p^2)}}\,\mathrm{Im}\,\phi_2^{\mathrm{had}}(s, 0). \tag{28}$$

The first measurements of $\Delta\sigma_T$ were in the early 1970's and significant nonzero values were measured in the region of $2.3 \le \sqrt{s} \le 3.6$ GeV [46]. Subsequent measurements for $\sqrt{s} < 2.3$ GeV revealed a rich structure. This structure was interpreted as evidence for the formation of diproton resonances. $\Delta\sigma_T$ data decrease rapidly with increasing $\sqrt{s}$

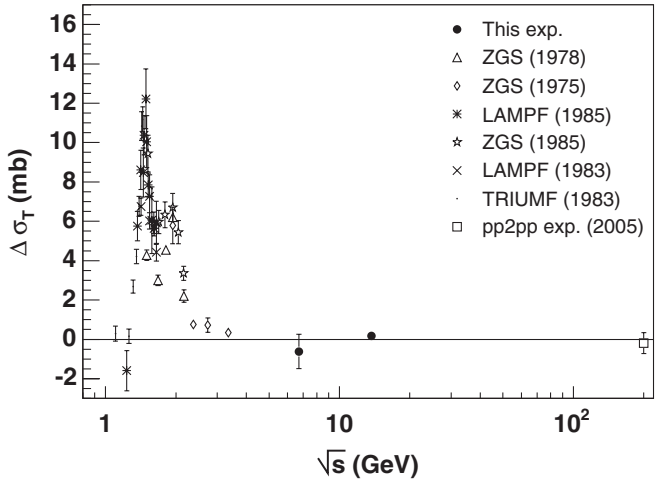

FIG. 19. $\Delta\sigma_T$ as a function of $\sqrt{s}$. Our results are shown as filled circles at $\sqrt{s} = 6.8$ GeV and $\sqrt{s} = 13.7$ GeV.

and results consistent with zero at $\sqrt{s} = 200$ GeV [30] agree with this extrapolation.

We estimate $\Delta\sigma_T$ from A_{NN} data at $\sqrt{s} = 6.8$ and 13.7 GeV. As discussed for Eq. (26), r_2 is assumed to have no $-t$ dependence. Therefore, Im r_2 directly connects to $\Delta\sigma_T$ as

$$\Delta\sigma_T = -2\,\mathrm{Im}\, r_2 \times \sigma_{\mathrm{tot}}, \tag{29}$$

where σ_{tot} is the unpolarized total cross section as in (5). We use $\sigma_{\mathrm{tot}} = 38.4 \pm 0.05$ mb for both energies reported here.

Results are

$$\Delta\sigma_T = -1.253 \pm 0.875\ (\mathrm{mb}) \tag{30}$$

for $\sqrt{s} = 6.8$ GeV and

$$\Delta\sigma_T = 0.016 \pm 0.232\ (\mathrm{mb}) \tag{31}$$

for $\sqrt{s} = 13.7$ GeV. The results are consistent with zero. Figure 19 displays $\Delta\sigma_T$ as a function of $\sqrt{s}$. Our results are shown as filled circles. Previous measurements are also shown, including the RHIC colliding beam measurement at $\sqrt{s} = 200$ GeV [30]. Our results are consistent with the extrapolation of lower energy data, with $\Delta\sigma_T \to 0$ for $\sqrt{s} > 4$ GeV.

V. CONCLUSION

We have presented results for the transverse single-spin and double-spin asymmetries, A_N and A_{NN}, in pp elastic scattering in the region $0.001 < -t < 0.032$ $(\mathrm{GeV}/c)^2$ using the RHIC polarized proton beam and a polarized atomic hydrogen gas jet target.

A_N data were presented for $\sqrt{s} = 6.8$ GeV, for nine $-t$ bins in the CNI regions, with 10% accuracy. The systematic uncertainties are smaller than the statistical uncertainties. The A_N data indicate the presence of a nonzero single spin-flip hadronic amplitude $\phi_5^{\mathrm{had}}(s, t)$ at this energy and suggest a significant $\sqrt{s}$ dependence for this amplitude, when compared with previously published data at $\sqrt{s} = 13.7$ GeV. A theoretical model for *proton-proton* elastic scattering, using Regge pole exchange for f, a_2, ω, ρ, and the Pomeron, predicted a nonzero hadronic spin-flip amplitude at $\sqrt{s} = 6.8$ GeV based on *proton-carbon* elastic scattering data and the previously published result for *proton-proton* at $\sqrt{s} = 13.7$ GeV. This prediction is consistent with our data. Following this theoretical description, the Pomeron is found to have nonzero coupling to $\phi_5^{\mathrm{had}}(s, t)$ [15].

A_{NN} data for $\sqrt{s} = 6.8$ GeV and 13.7 GeV were also presented. The measured A_{NN} data points, vs $-t$, are small. The mean values $\langle A_{NN}\rangle$ in the region of $0.001 < -t < 0.032$ $(\mathrm{GeV}/c)^2$ are small for $\sqrt{s} = 6.8$ GeV and consistent with zero for $\sqrt{s} = 13.7$ GeV. Consequently, our data do not support a sizable double spin-flip hadronic amplitude $\phi_2^{\mathrm{had}}(s, t)$ at these energies.

Based on the A_{NN} data, we have presented estimates of $\Delta\sigma_T$ at $\sqrt{s} = 6.8$ GeV and 13.7 GeV. The $\Delta\sigma_T$ values are consistent with zero for both energies. These data are also consistent with previous results where a significant $\Delta\sigma_T$ was observed in the range $\sqrt{s} = 1.7$–3 GeV, and a value consistent with zero was reported at $\sqrt{s} = 200$ GeV.

ACKNOWLEDGMENTS

We would like to thank the Instrumentation Division and Collider Accelerator Department at BNL for their work on the silicon detectors, electronics, and the RHIC polarized proton beam. We also would like to thank T. L. Trueman for useful discussions. This work is performed under the auspices of U.S. DOE Contract No. DE-AC02-98CH10886 and No. W-31-109-ENG-38, DOE Grant No. DE-FG02-88ER40438, NSF Grant No. PHY-0100348, and with support from RIKEN, Japan.

[1] S. Nussinov, Phys. Rev. Lett. **34**, 1286 (1975); Phys. Rev. D **14**, 246 (1976).
[2] M. I. Goldberger *et al.*, Phys. Rev. **120**, 2250 (1960).
[3] T. L. Trueman (private communication).
[4] N. H. Buttimore, E. Gotsman, and E. Leader, Phys. Rev. D **18**, 694 (1978).

[5] R. Cahn, Z. Phys. C **15**, 253 (1982).
[6] R. E. Breedon *et al.*, Phys. Lett. B **216**, 459 (1989).
[7] N. H. Buttimore, B. Z. Kopeliovich, E. Leader, J. Soffer, and T. L. Trueman, Phys. Rev. D **59**, 114010 (1999).
[8] N. H. Buttimore, E. Leader, and T. L. Trueman, Phys. Rev. D **64**, 094021 (2001).
[9] B. Z. Kopeliovich and L. I. Lapidus, Sov. J. Nucl. Phys. **19**, 114 (1974).
[10] O. V. Selyugin, Mod. Phys. Lett. A **12**, 1379 (1997); Phys. Rev. D **60**, 074028 (1999).
[11] B. Z. Kopeliovich and B. G. Zakharov, Phys. Lett. B **226**, 156 (1989).
[12] C. Bourrely, J. Soffer, and T. T. Wu, Phys. Rev. D **19**, 3249 (1979); Nucl. Phys. **B247**, 15 (1984).
[13] C. Bourrely, H. A. Neal, H. A. Ogren, J. Soffer, and T. T. Wu, Phys. Rev. D **26**, 1781 (1982).
[14] C. Bourrely, J. Soffer, and T. T. Wu, Phys. Rev. D **76**, 053002 (2007).
[15] T. L. Trueman, Phys. Rev. D **77**, 054005 (2008).
[16] J. R. Cudell *et al.*, Review of Particle Physics **592**, 313 (2004).
[17] M. Ross *et al.*, Nucl. Phys. **B23**, 269 (1970); F. Henyey *et al.*, Phys. Rev. **182**, 1579 (1969); G. L. Kane and A. Seidl, Rev. Mod. Phys. **48**, 309 (1976).
[18] *Proceedings of the International Symposium on Polarization Phenomena of Nucleons, Basel 1960*, edited by P. Huber and K. P. Meyer (Birkhäuser Verge, Basel and Stuttgart, 1961).
[19] J. Schwinger, Phys. Rev. **73**, 407 (1948).
[20] N. Akchurin *et al.*, Phys. Rev. D **48**, 3026 (1993).
[21] S. Bültmann *et al.*, Phys. Lett. B **632**, 167 (2006).
[22] H. Okada *et al.*, Phys. Lett. B **638**, 450 (2006).
[23] J. Tojo *et al.*, Phys. Rev. Lett. **89**, 052302 (2002).
[24] O. Jinnouchi *et al.*, *Proc. 16th International Spin Physics Symposium SPIN2004*, p. 515.
[25] A. Bravar *et al.*, Nucl. Phys. B, Proc. Suppl. **146**, 77 (2005).
[26] E. Leader and T. L. Trueman, Phys. Rev. D **61**, 077504 (2000).
[27] T. L. Trueman, arXiv:hep-ph/0604153.
[28] J. R. O'Fallon *et al.*, Phys. Rev. Lett. **39**, 733 (1977); D. G. Crabb *et al.*, Phys. Rev. Lett. **41**, 1257 (1978).
[29] F. Halzen and G. H. Thomas, Phys. Rev. D **10**, 344 (1974).
[30] S. Bültmann *et al.*, Phys. Lett. B **647**, 98 (2007).
[31] Y. Akimov *et al.*, Sov. Phys. JETP **21**, 507 (1965); G. Beznogikh *et al.*, Phys. Lett. B **30**, 274 (1969); V. Bartenev *et al.*, Phys. Rev. Lett. **31**, 1088 (1973).
[32] H. Okada, Doctoral thesis, 2006; http://www.bnl.gov/userscenter/Thesis/2007/Okada_Thesis.pdf
[33] A. Zelenski *et al.*, Nucl. Instrum. Methods Phys. Res., Sect. A **536**, 248 (2005).
[34] A. Zelenski *et al.*, *Proc. 16th International Spin Physics Symposium SPIN2004*, p. 761.
[35] A. Nass *et al.*, *Proc. 16th International Spin Physics Symposium SPIN2004*, p. 776.
[36] T. Wise *et al.*, *Proc. 16th International Spin Physics Symposium SPIN2004*, p. 757.
[37] T. Wise *et al.*, Nucl. Instrum. Methods Phys. Res., Sect. A **556**, 1 (2006).
[38] Y. Makdisi *et al.*, *Proc. 17th International Spin Physics Symposium SPIN2006*, p. 975.
[39] D. Svirida *et al.*, *Proc. 16th International Spin Physics Symposium SPIN2004*, p. 722.
[40] http://physics.nist.gov/PhysRefData/Star/Text/contents.html.
[41] G. G. Ohlsen and P. W. Keaton, Nucl. Instrum. Methods **109**, 41 (1973).
[42] http://pdg.lbl.gov/2006/hadronic-xsections/hadron.html.
[43] U. Amaldi *et al.*, Phys. Lett. B **36**, 504 (1971); N. Amos *et al.*, Phys. Lett. B **128**, 343 (1983); M. Holder *et al.*, Phys. Lett. B **36**, 400 (1971); V. Bartenev *et al.*, Phys. Rev. Lett. **29**, 1755 (1972); **31**, 1088 (1973); G. Barbiellini *et al.*, Phys. Lett. B **39**, 663 (1972); N. Amos *et al.*, Phys. Lett. B **120**, 460 (1983); K. J. Foley *et al.*, Phys. Rev. Lett. **11**, 425 (1963); L. A. Fajardo *et al.*, Phys. Rev. D **24**, 46 (1981); Kh. M. Chernev *et al.*, Phys. Lett. B **36**, 266 (1971).
[44] P. R. Cameron *et al.*, *Proc. 99 Particle Accel. Conf.* (IEEE, New York, 1999), p. 2146, Cat. No. 99CH36366.
[45] We also applied a fit for four free parameters; Re r_2, Im r_2, Re r_5, and Im r_5. We concluded that the uncertainty from the contribution from r_5 was negligible.
[46] Ed. K. Biegert *et al.*, Phys. Lett. B **73**, 235 (1978); W. P. Madigan *et al.*, Phys. Rev. D **31**, 966 (1985); W. R. Ditzler *et al.*, Phys. Rev. D **27**, 680 (1983); J. P. Stanley *et al.*, Nucl. Phys. A **403**, 525 (1983).